Article

Cell Reports

Piezo regulates epithelial topology and promotes precision in organ size control

Graphical abstract

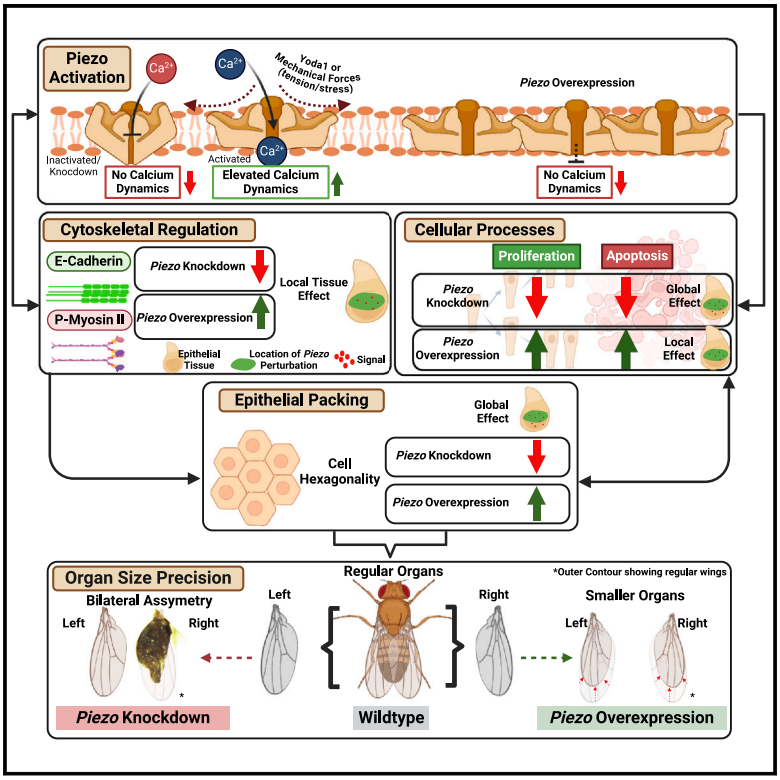

Highlights

- Piezo regulates the bilateral precision of organ size
- Piezo's functions include phenotypic effects that span from cells to tissues
- Piezo regulates emergent tissue-level properties both locally and non-locally
- A computational model shows Piezo's role in linking subcellular processes to growth

Authors

Mayesha Sahir Mim, Nilay Kumar, Megan Levis, ..., David Gazzo, Trent Robinett, Jeremiah J. Zartman

Correspondence

jzartman@nd.edu

In brief

Mim et al. show that Piezo regulates organ size and cell topology by controlling cell tension, cell division, cell death, and tissue properties both locally and non-locally. Piezo ensures precise organ growth by regulating cellular processes and tissue architecture through tension-mediated feedback control of cell division and elimination.

Mim et al., 2024, Cell Reports *43*, 114398
July 23, 2024
https://doi.org/10.1016/j.celrep.2024.114398

CellPress

Cell Reports

CellPress
OPEN ACCESS

Article

Piezo regulates epithelial topology and promotes precision in organ size control

Mayesha Sahir Mim,[1,2,4] Nilay Kumar,[1,4] Megan Levis,[1,2] Maria F. Unger,[1] Gabriel Miranda,[1] David Gazzo,[1,2] Trent Robinett,[1] and Jeremiah J. Zartman[1,2,3,5,*]

[1]Department of Chemical and Biomolecular Engineering, University of Notre Dame, Notre Dame, IN 46556, USA
[2]Bioengineering Graduate Program, University of Notre Dame, Notre Dame, IN 46556, USA
[3]Department of Biological Sciences, University of Notre Dame, Notre Dame, IN 46556, USA
[4]These authors contributed equally
[5]Lead contact
*Correspondence: jzartman@nd.edu
https://doi.org/10.1016/j.celrep.2024.114398

SUMMARY

Mechanosensitive Piezo channels regulate cell division, cell extrusion, and cell death. However, systems-level functions of Piezo in regulating organogenesis remain poorly understood. Here, we demonstrate that Piezo controls epithelial cell topology to ensure precise organ growth by integrating live-imaging experiments with pharmacological and genetic perturbations and computational modeling. Notably, the knockout or knockdown of *Piezo* increases bilateral asymmetry in wing size. Piezo's multifaceted functions can be deconstructed as either autonomous or non-autonomous based on a comparison between tissue-compartment-level perturbations or between genetic perturbation populations at the whole-tissue level. A computational model that posits cell proliferation and apoptosis regulation through modulation of the cutoff tension required for Piezo channel activation explains key cell and tissue phenotypes arising from perturbations of Piezo expression levels. Our findings demonstrate that Piezo promotes robustness in regulating epithelial topology and is necessary for precise organ size control.

INTRODUCTION

How organ size is controlled precisely in animals remains poorly understood. The final size and shapes of organs are influenced by multiple factors that include regulation of cellular processes such as proliferation or apoptosis combined with cytoskeletal regulation generating forces within the cell.[1,2] Coordinated regulation between these processes is critical to maintaining the desired packing of single cells as the organ grows. Proper cell packing during organ development is required for the transformation of the 2D epithelial sheet into a 3D organ.[3–8] Changes in epithelial packing at early developmental stages have been associated with severe phenotypic changes in the final organ morphology.[9,10] As a second messenger, cytoplasmic calcium (Ca^{2+}) plays a crucial role in mediating these single-cell processes.[11,12] Further, gap-junction communication results in multicellular Ca^{2+} dynamics. Tissue-level Ca^{2+} waves correlate with a reduction in final organ size and changes in cytoskeletal regulation, while localized Ca^{2+} spiking occurs downstream of insulin signaling and correlates with growth. While studies have investigated the role of cell mechanics in regulating organ size,[13,14] how mechanical activation of Ca^{2+} signaling impacts organ size control still remains poorly understood. In this work, we report that the mechanosensitive channel Piezo, an upstream regulator of cytosolic Ca^{2+} signaling dynamics, regulates epithelial topology and ensures precision in regulating the final organ size.

Through mechanotransduction, mechanical forces are converted into biochemical signals through a cascade of molecular reactions. This process is mediated by the concerted activities of cell membrane, cytoskeleton, and extracellular matrix (ECM) proteins.[15–19] As key mechanotransducers, Piezo proteins are multidomain, transmembrane mechanosensitive ion channels containing over 2,000 amino acids.[20] The trimeric Piezo channel complex is shaped like a propeller with three blades organized around a central pore, which is lined with amino acids to filter and gate the passage of ions.[21] Piezo1 ion channel molecules can bend the local lipid environment in cell membranes to form dome-like structures, which likely contributes to the mechanosensitivity of these channels.[22] In mammals, Piezo1 is expressed in most cell types, while Piezo2 is primarily expressed in neural tissues.[20] Piezo channels are activated by mechanical force. Piezo1 activation occurs at force-producing adherens junctions, leading to an influx of Ca^{2+} into the cells.[23] This Ca^{2+} can originate from either the extracellular space or within-cell Ca^{2+} storage sites, such as the endoplasmic reticulum (ER). Consequently, this ion flow changes the cell's electrical activity and can activate downstream signaling pathways such as the protein kinase C (PKC), mitogen-activated protein kinase (MAPK), or nuclear factor of activated T cells (NFAT) pathways.[24–26]

Recently, Piezo has been identified as a key regulator of tissue homeostasis.[27] In several epithelial systems, Piezo1 regulates ERK1/2-mediated cell-cycle progression from the G2 to the

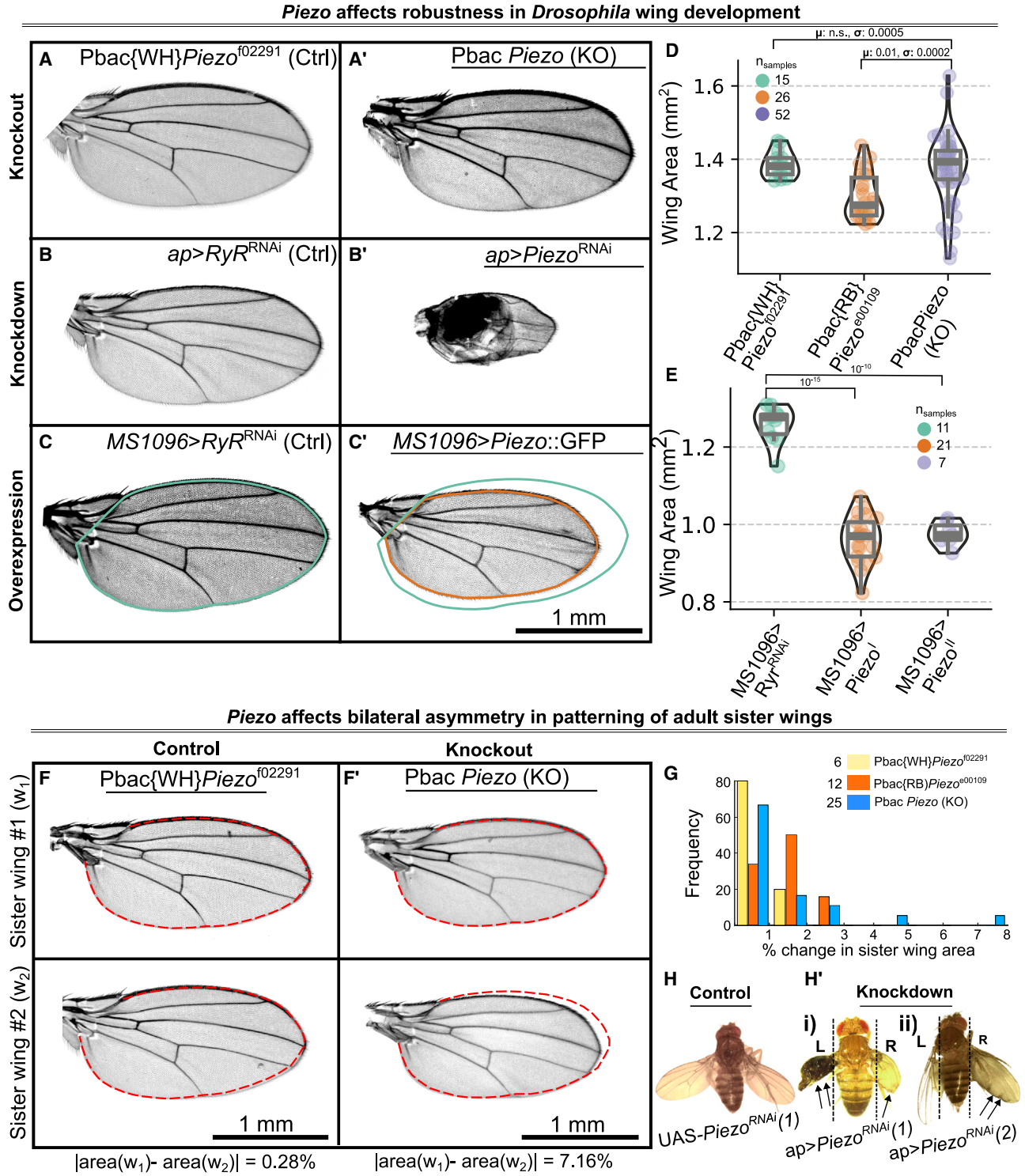

Figure 1. Piezo determines size precision in bilateral organs

(A and A′) *Drosophila* wings from a *Piezo*-knockout line do not exhibit significant changes in average wing size compared to the control line used to generate the knockout line.

(B and B′) Adult *Drosophila* wings generated using RNAi-mediated knockdown of *Piezo* and a previously validated corresponding control cross.

(C and C′) Overexpression of *Piezo* in the wing disc results in smaller wings compared to control discs targeting a non-expressed gene with no observed phenotype. The reduction in wing area is visualized by comparing the outline of control wings (orange) with that of Piezo-overexpressed wings (green).

(legend continued on next page)

mitotic (M) phase, initiating mitosis, Ca^{2+}-flux-mediated cell proliferation,[28] or cell extrusion to relax stress from overcrowding via the Rho signaling pathway.[29] Several studies show that Piezo channels regulate apoptosis by sensing mechanical stress and inducing changes in intracellular Ca^{2+} levels, which activate downstream signaling pathways involved in programmed cell death.[30] Piezo also regulates actin dynamics, Ca^{2+}-facilitated actin stress fiber formation, and integrin signaling. In particular, Piezo colocalizes with E-Cadherin-β-catenin and activates integrin-FAK signaling through focal adhesion.[31–33] Piezo also regulates cell-fate determination and diverse aspects of morphogenesis and organogenesis, including embryonic development, tissue regeneration and cell migration, cardiovascular development, axon growth in the brain, and bone formation from the embryonic stages, depending on *Piezo* expression and activation.[34–39] To ensure tissue regeneration, Piezo promotes the proliferation and differentiation of stem cells.[40] Piezo also regulates cell migration by guiding the movement of cells during development.[41] Despite Piezo's multifaceted roles in development, a holistic, integrative mechanism that explains how Piezo channels contribute to the regulation of organogenesis is still not fully formulated.

Of note, there is a gap of knowledge in understanding Piezo's role in epithelial morphogenesis.[40,42–44] Mechanotransduction-led entry of Ca^{2+} into cells triggers multiple cell-level processes whose context in development and size regulation is still unclear. For example, much remains to be discovered about how these ion channels regulate Ca^{2+} activity within complex multicellular epithelial tissues. Recent works highlighting the existence and role of multiple dynamical IP_3-signaling-mediated Ca^{2+} patterns in regulating organ size make it critically important to understand the role of Piezo in epithelial morphogenesis and homeostasis.[45] To bridge this gap, *Drosophila melanogaster* is a rapid and inexpensive hypothesis-testing model for genetically driven biomechanical processes such as cancer and morphogenesis.[46] Based on sequence structure, the single Piezo homolog of *Drosophila*, Piezo, is homologous to both Piezo1 and Piezo2.[43,47]

Here, we examined Piezo's function in the *Drosophila* wing disc. We report that Piezo is required for bilateral symmetry in the adult wings of *Drosophila*. Relative levels of *Piezo* expression impact the Ca^{2+} dynamics in the wing imaginal disc of *Drosophila* larvae. Piezo also regulates the proper distribution of E-Cadherin and phosphorylated non-muscle myosin II (pMyoII). Both *Piezo* overexpression and *Piezo* inhibition impact the rates of cell proliferation and apoptosis. To analyze the homeostatic regulation further, we demonstrate that increased overcrowding occurs when *Piezo* is knocked down. In contrast, overexpression of *Piezo* decreases crowding as measured by an increase in hexagonality in epithelial packing. Thus, Piezo plays an important role in the precision of organ size control through the integration of multiple roles as a homeostatic regulator of the tension thresholds controlling proliferation and apoptosis.

RESULTS

Piezo regulates precision of bilateral symmetry of *Drosophila* wings

Drosophila has a single homolog, Piezo, to the mammalian Piezo1.[47] To investigate potential roles of Piezo in organ size control, we used the GAL4-UAS binary gene expression system to knock down (KD) with $Piezo^{RNAi}$ or overexpress (OE) *Piezo* in the wing imaginal disc. We also characterized the complete knockout (KO) of the *Piezo* line to compare with the GAL4-UAS-driven perturbations. Surprisingly, while KO of *Piezo1* is lethal in mice and other model systems,[39,48,49] *Drosophila* not only remains viable on KO of *Piezo* but also develops with wings that do not show severe phenotypic defects (Figures 1A and 1A′). In addition, the mean wing area resulting from *Piezo* KO remained unchanged compared to the parental lines used to generate the KO line (statistics in Table S2). Surprisingly, quantifying the *Piezo*-KO wing sizes showed a significant increase in within-population variability (statistics in Table S2; Figure 1D).

We also knocked down the mRNA expression of *Piezo* by expressing an RNA-interference (RNAi) construct targeting *Piezo* in the dorsal compartment with Apterous-GAL4>$Piezo^{RNAi}$. KD of *Piezo* led to adults with severe morphological defects, including necrotic blisters in the wings, compared to control (Figures 1B and 1B′). Serving as a negative control of a gene not expressed in the wing disc and lacking any phenotype,[50–52] *Ryr* was knocked down, as it is not significantly expressed in the epithelial wing disc cells and produces morphologically normal progeny, using RNAi by crossing the parental Gal4 lines to UAS-RyR^{RNAi}.[50,52] Surprisingly, the severity of phenotypic traits was weaker in the KO versus the KD lines. This suggests a possibility of genetic compensation, where a similarly functioning protein takes up the role of the downregulated component.[42] Another potential explanation for these differences is an unexpected RNAi-mediated off-target effect. However, the Vienna Drosophila Resource Center (VDRC) does not predict off-target effects with the UAS-$Piezo^{RNAi}$ line used.[53] Further, several previous publications have used this UAS-$Piezo^{RNAi}$ line.[31,54–57] Last, we used an *MS1096*-Gal4 driver to OE these

(D) *Piezo*-knockout wings exhibit significant heterogeneity in wing size compared to the original Piggybac lines used to generate the knockout. Bee-swarm plot showing the distribution of wing area for different perturbations to *Piezo*. KO represents the *Piezo*-knockout line *p* value comparing means, and variances of populations are indicated over the solid lines.

(E) Bee-swarm plot showing the quantified distribution of wing area for overexpression of *Piezo*. Superscripts I and II against the *Piezo* label indicate two different overexpression lines (detailed in the STAR Methods). Bonferroni correction was employed for statistical analysis. For explanation of the bee-swarm plots, see Figure S2.

(F and F′) Sister wings belonging to the control and *Piezo*-knockout lines demonstrate significant variation between bilateral organs. Red lines have been used to outline the contour of a sister wing. The same contour has been overlaid as dashed red lines for the other sister wing. All scale bars, 1 mm.

(G) Bar graph showing the distribution of differences in the area between sister wings of the Piezo-knockout versus knockdown lines.

(H) Adult UAS-Ryr^{RNAi} fly (control) and (H′) adult *ap*>$Piezo^{RNAi}$ fly showing significant patterning and symmetry defects between each two wings. *Piezo* knockdown (KD) caused (H′i) a tumorous and pigmentation phenotype and (H′ii) a less severe blister phenotype using two independent RNAi lines. See also Figures S1–S3.

receptors predominantly in the dorsal compartment of the wing disc using two UAS-*Piezo*::GFP fly lines. We report a nearly 25% reduction in wing area observed consistently using two different commercially available and previously validated UAS-*Piezo*-overexpressing lines (Figures 1C, 1C′, and 1E; Table S3). Similar organ area reduction was corroborated for *Piezo* overexpression using an independent UAS-*Piezo* line without a GFP tag crossed to *MS1096*-Gal4 (Figure S3).

Further, we used multiple independent Gal4 lines to aid in discriminating between any Gal4-specific effects. As some Gal4 lines include a UAS-GFP component, an alternative was used to characterize *Piezo*-GFP levels. Employing various Gal4 drivers in these experiments was done to ensure more rigorous assessments of phenotypes. The *Apterous* (*ap*) Gal4 driver, which drives expression only on the dorsal compartment of tissue, also incorporates GFP expression, which made it challenging to segregate flies overexpressing *Piezo*-GFP, as there were two GFP constructs to distinguish. The *MS1096*-Gal4 driver, which also drives expression predominantly on the dorsal compartment, did not independently express GFP, which allowed us to sort larvae based on the presence of GFP. Consequently, we selected *MS1096* for *Piezo* overexpression. However, the *Piezo*^{RNAi} line did not have a GFP tag, making it easier to perturb only the dorsal compartment of the wing disc with the *ap-Gal4* using its GFP tag. For a comparable experiment, our objective was to overexpress *Piezo* predominantly in the dorsal compartment, making *MS1096* the most appropriate choice for the Gal4 driver.

Additional analysis revealed that KO of *Piezo* significantly increases fluctuating asymmetry in sister wings (comparing wings from the same fly) (Figures 1F and 1F′). These asymmetries between sister wings are qualitatively notable in certain cases (Figure 1G). Interestingly, partial KD of *Piezo* in the dorsal compartment of the wing disc enhanced these differences in adult morphologies of sister wings (Figure 1H′). These KD flies exhibited asymmetry in left and right wings with severe tumorous and blister-like defects, observed using two independent *Piezo*-KD lines in parallel to avoid off-target effects, compared to the parental control (Figures 1H and H′). Taken together, these results suggest that Piezo plays a significant role in regulating the left-right symmetry and precision of organ growth.

Expression of *Piezo* impacts the frequency of Ca^{2+} spiking in wing discs

As Piezo is a Ca^{2+}-permeable channel, the regulation of organogenesis through Piezo is likely related to the Ca^{2+} signaling pathway, given the vital roles that Ca^{2+} plays in development.[11,58] However, the exact mechanism by which Piezo-stimulated Ca^{2+} signaling regulates robustness in growth and patterning remains unclear. The selective Piezo1 agonist, Yoda1,[59] enables the study of downstream effects of Piezo1 without external mechanical activation. Piezo is ubiquitously present in mammalian cells[60] and in the wing imaginal disc of *Drosophila melanogaster* (Figure S1). Hence, to study the role of endogenous Piezo in regulating Ca^{2+} dynamics, wing imaginal discs that express the genetically encoded Ca^{2+} sensor GCaMP6f[61] were treated with 1 mM Yoda1 with an initial incubation period of 45 min. The administration of Yoda1 significantly increased the population of cells displaying spikes in Ca^{2+} activity compared to vehicle control (DMSO) treatment (Figures 2A and 2A′; Videos S1 and S2). This led to a high-frequency Ca^{2+} response with an average of about 7 ± 10 peaks per 1,000 s for randomly selected spiking cells (Figure 2D). Spiking frequency first increased and then eventually decreased as the treatment period increased (Figure 2D; Videos S7–S10).

We next tested if the origin of these Yoda1-mediated Ca^{2+} spikes is through activation of the Piezo channel. Downregulation of *Piezo* in the wing imaginal discs led to an effectively complete loss of high-frequency Ca^{2+} spikes despite treatment of Yoda1 (*nubbin*>GCaMP6f x UAS-*Piezo*^{RNAi}, Figures 2B and 2B′; Videos S3 and S4). Surprisingly, spikes of cytosolic Ca^{2+} also significantly decreased in discs that overexpressed *Piezo*::GFP, both in vehicle-control conditions (Figure 2C; Video S5) and when stimulated by Yoda1 for an extended period (Figure 2C′; Video S6). These results demonstrate the involvement of Piezo in the direct regulation of Ca^{2+} dynamics in wing discs. Interestingly, we found a biphasic relationship between Ca^{2+} spiking activity and Piezo expression levels.

The presence of a large population of cells exhibiting a high-frequency Ca^{2+} response when stimulated by Yoda1 suggests ubiquitous expression of Piezo within the pouch. This is consistent with the expression of Piezo reported in the modENCODE dataset.[63] This confounding observation of both overexpression and inhibition of *Piezo* leading to a loss in Ca^{2+} activity suggests possible interactions between Piezo1 and the IP_3 signaling pathway to maintain optimal Ca^{2+} signaling levels within the pouch (i.e., the "Goldilocks zone" of optimal activity).[45] To test this question, we adapted a two-pool model of Ca^{2+} signaling to predict the conditions upon which the opening of Ca^{2+} channels can induce a high-frequency Ca^{2+} oscillatory response.[62] We numerically solved the model by varying the parameter υ_{max} that controls the rate of extracellular Ca^{2+} entry through ion channels into the cytosolic volume (Figure 2E). We also tested coincubation of an IP_3 receptor antagonist, 200 μM 2-APB (2-aminoethoxydiphenyl borate),[64] along with 1 mM Yoda1, which blocked store-operated Ca^{2+} influx as well as the Piezo-mediated Ca^{2+} spiking dynamics (Figure 2; Video S11). For low υ_{max} values, the computational model shows that cells do not exhibit stochastic spikes in Ca^{2+} (Figure 2F). Low υ_{max} values correspond to the cases where *Piezo* is knocked down from the system, as a lack of *Piezo* expression reduces the rates of extracellular Ca^{2+} entry within the cytosol. On the other hand, recent studies using gastric cancer cells report an increase in Ca^{2+} influx upon *Piezo1* overexpression.[65] Thus, overexpression of *Piezo* corresponds to a simulated scenario of increased υ_{max} values.

We also show that the frequency of Ca^{2+} oscillations predicted by the model upon ion channel activation is comparable to the frequency of oscillations from Yoda1-mediated activation of Piezo (Figures 2D and 2F). Further, the model predicts that either low Piezo expression levels (low υ_{max}) or high Piezo expression levels (high υ_{max}) resulted in minimal Ca^{2+} spiking when the channel was stimulated exogenously. Taken together, the non-intuitive and non-linear dynamical response of Ca^{2+} signaling activity with variation in *Piezo* expression levels is consistent with a two-pool model of Piezo-regulated Ca^{2+} signaling.

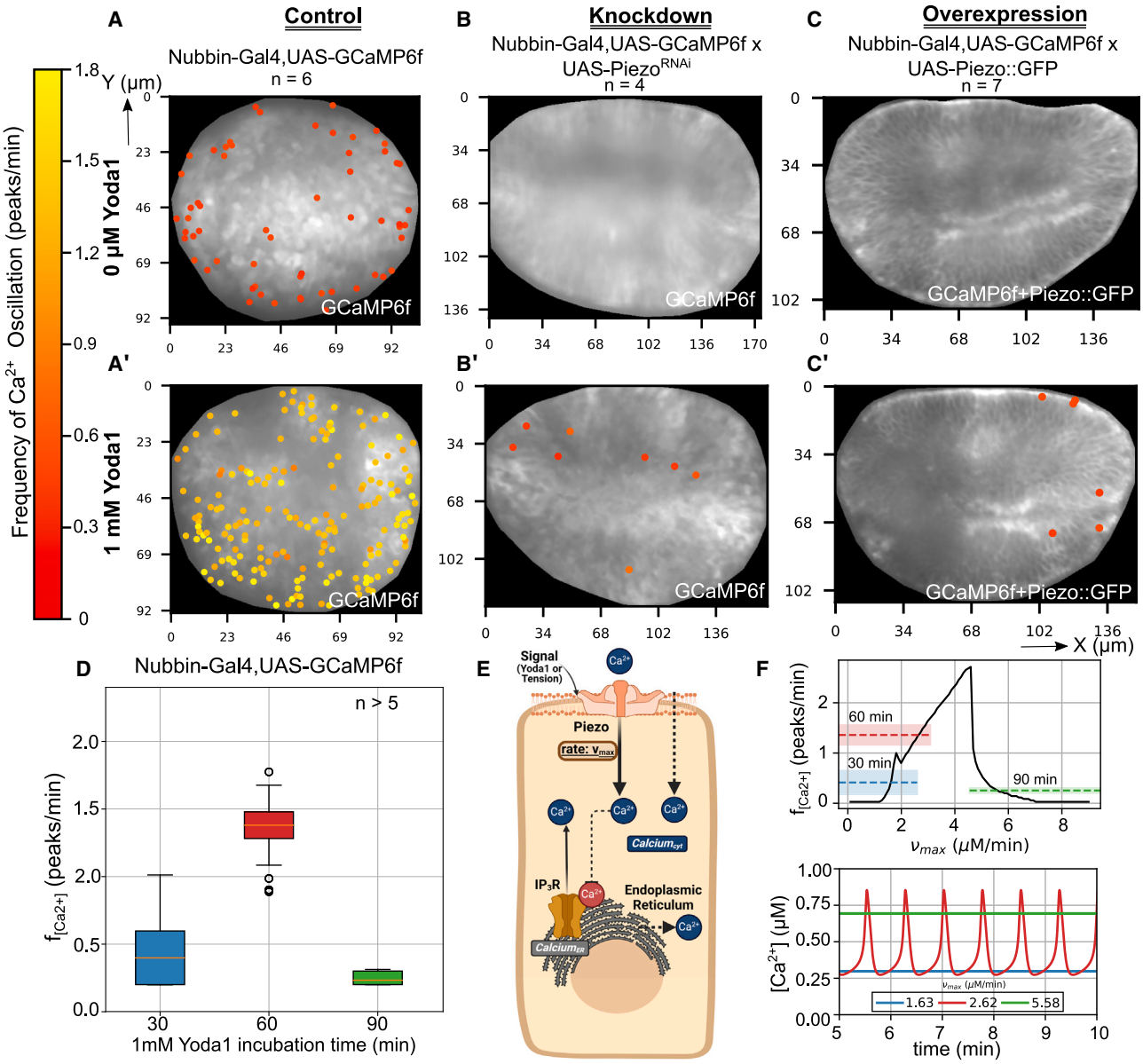

Figure 2. Divergent and spatial effects of Piezo activity on Ca^{2+} spiking activity

(A–C′) Heatmaps of imaginal discs expressing GCaMP6f cultured in low-ecdysone Grace's medium with (A, B, and C) vehicle control (DMSO) or (A′, B′, and C′) Yoda1. (A and A′) Control discs expressing the GCaMP6f Ca^{2+} sensor ($n = 6$). (B and B′) Knockdown of *Piezo* prevents Ca^{2+} response to Yoda1 ($n = 4$). (C and C′) Overexpression of *Piezo* ($n = 7$). Imaging was done after an incubation time of 30 min for 5–10 min for all cases ($n = 6$ for each case). Scales are included for each individual case in micrometers.

(D) Plot showing variation in Ca^{2+} frequency over time when imaged for 30, 60, and 90 min. Data are represented as the mean ± SEM.

(E) A schematic of the two-pool Ca^{2+} signaling model.[62] Parameter υ_{max}, controlling the entry of extracellular Ca^{2+} within the cytosol, was increased, and the number of peaks in Ca^{2+} activity in response to variation of υ_0 was plotted.

(F) Increased ν_{max} causes saturation of cytosolic Ca^{2+} levels similar to *Piezo* overexpression. (Top) Frequency variation of Ca^{2+} oscillations (f[Ca^{2+}]) with increasing flux of [Ca^{2+}] (ν_{max}) from the extracellular space to the cytosol. The horizontal colors correspond to the frequency variation in discs with increasing incubation times of Yoda1. Dashed lines indicate the mean of frequency, while the shaded area represents the standard deviation. (Bottom) Model-generated Ca^{2+} responses for different values reflect the Ca^{2+} oscillations observed in experimental results. ν_{max} values in the bottom graph were parsed from the experimental results (top). See also Figure S10.

In our experimental results, upon increasing the treatment period with Yoda1 or overexpressing Piezo, there is a concurrent increase in the number of channels expressed within the cells. Consequently, when a cell undergoes stretching, the increased number of channels contributes to an overall elevation in Ca^{2+} flux. This is reflected in an increase in υ_{max} in the two-pool model.

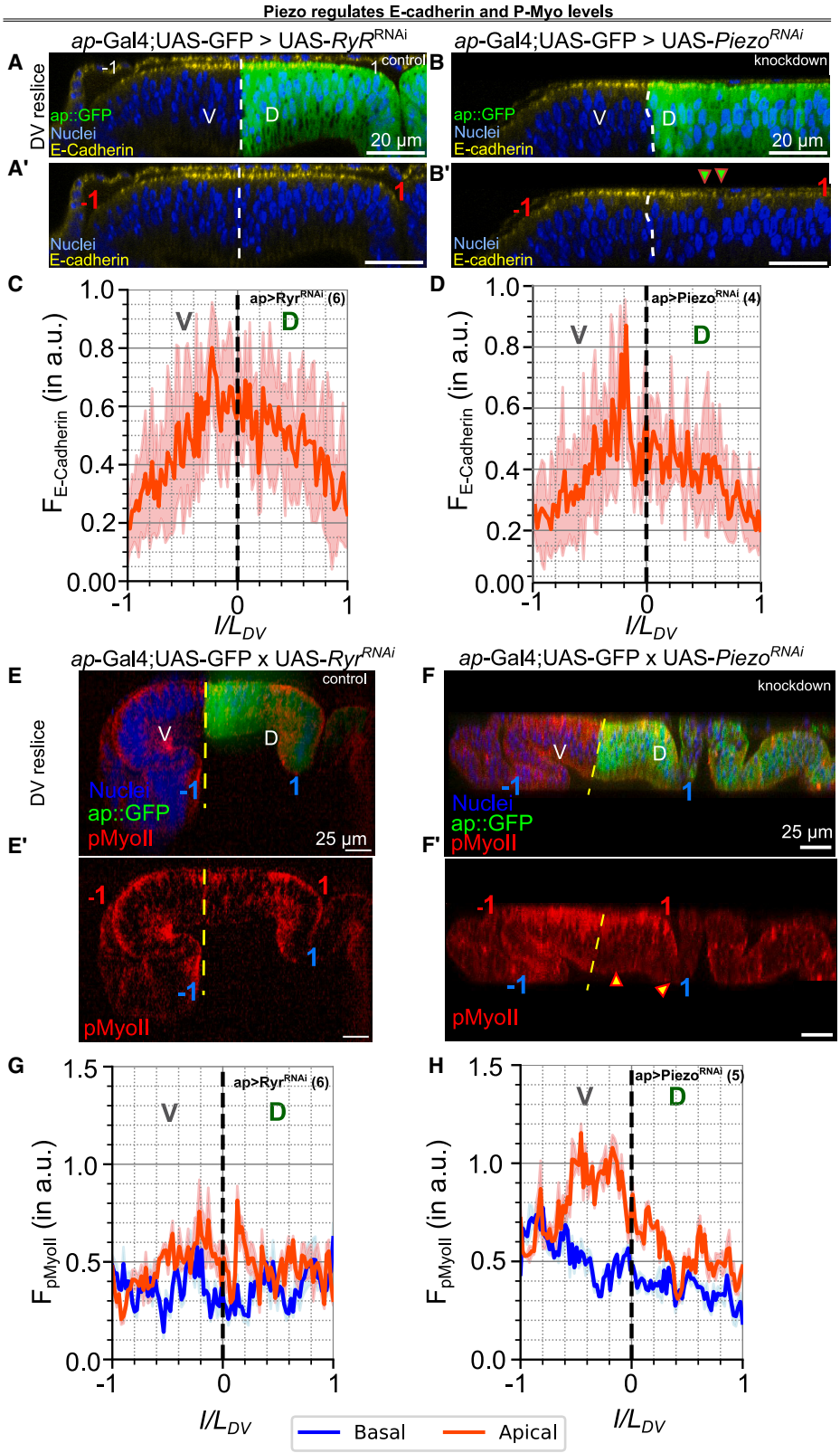

(legend on next page)

In summary, the incremental adjustment of υ_{max} from 0 to the maximum value in our study effectively simulates the transition from KD to overexpression of *Piezo* (Figures 2B, 2C, 2E, and 2F). More details about the model are included in the STAR Methods.

In turn, this non-linear Ca^{2+} response is critical in interpreting how Piezo regulates active cell-level processes such as cell proliferation, death, and patterning of mechanical forces. This result suggests that both loss-of-function and gain-of-function perturbations to *Piezo* expression may, in some cases, produce similar phenotypic effects for different mechanisms.

Piezo regulates apical-basal tension, cell proliferation, and apoptosis within the developing epithelium

To investigate how Piezo impacts the precision of growth and morphogenesis, we quantified changes in cell tension, cell proliferation, and cell death upon perturbation of *Piezo* expression levels. We used the *ap*-Gal4 driver to overexpress or inhibit *Piezo* in the dorsal compartment of the wing disc. The genetically unperturbed ventral compartment provides an internal tissue-level control for evaluating whether the effects are more local or tissue-wide and non-autonomous. Similarly, we tested the *engrailed*-Gal4 (*en*-Gal4) driver to perturb Piezo expression specifically in the posterior compartment. In this study, we utilized an additional genetic background (*en>Ryr*^{RNAi}) as a negative control to compare between populations, as was used in previous studies, and wing imaginal discs do not have any detectable Ryr expression.[50,52] This enabled us to evaluate change in the whole pouch region similar to a global (G) tissue-wide, non-autonomous comparison.[66] We have included a summary of all *Piezo* perturbations and subsequently affected signaling, cytoskeletal components, or cellular topology parameters as Table S1.

RNAi-mediated inhibition of *Piezo* led to a compartment-specific reduction in E-Cadherin at the apical surface of the pouch compared to control (Figures 3A–3D, S4A, and S4B). E-Cadherin is critical for adhering cells near the apical surface to one another.[67] We also report a compartment-specific reduction in localization of pMyoII at the pouch apical and basal surface along the cross sections of the tissue (Figures 3E–3H and S4). E-Cadherin is localized along the subapical regions of epithelial cells, specifically at adherens junctions, where it facilitates robust cell-cell adhesion.[68,69] We observed downregulation of E-Cadherin near the compartment boundary when Piezo was inhibited with RNAi in the dorsal compartment (Figures 3B, 3B′, and S4B). We also quantified the cortical expression of pMyoII in the apical and basal regions of the cells. We found that knocking down *Piezo* in the dorsal compartment reduced pMyoII away from the central region of the tissue (Figures 3F, 3F′, 3H, S4D, S4G, and S4H). The actin-pMyoII complex is essential for generating contractile forces manifesting a bent shape and folds in the wing imaginal disc hinge domain,[70–72] and loss of this structure is also observed with *Piezo* KD (Figures 3F and S5). Interestingly, we also observed an analogous upregulation of E-Cadherin and pMyoII levels for Piezo overexpression in the posterior compartment (Figure S4'). E-Cadherin generally has a higher expression level in the central region of the wing disc, but interestingly, it has even higher peaks coinciding with the upregulation of Piezo expression near the central region of the wing disc pouch (Figures S4′A and S5Ai).

To study tissue-level forces, we performed laser ablation experiments to test for differences in cell mechanics under stimulation or inhibition of Piezo from small-molecule inhibition. Recoil velocities of the apical cell membranes were semi-automatically measured from discs treated with and without Yoda1 (Figure S6 and Videos S14 and S15; STAR Methods). The recoil velocities of cells after treatment with Yoda1 did not show a significant difference compared to the control (Figure S6). However, recoil velocities, a measure of cell tension with a higher recoil velocity indicative of higher tension, were reduced after laser ablation for discs treated with the non-specific inhibitor of Piezo, GsMTx4.[73] Based on this, we conclude that reducing recoil velocity upon GsMTx4-mediated inhibition of *Piezo* results in a loss of apical cell tension (Figure S6 and Videos S14 and S16). The observation correlates well with the loss of E-Cadherin resulting from the genetic KD of *Piezo*. Together, these results suggest Piezo as a regulator of apical-basal tension during *Drosophila* wing disc development.

As a homeostatic regulator, Piezo triggers both proliferation and apoptosis within Madin-Darby canine kidney (MDCK) cells.[29,74] To confirm whether this occurs in the wing disc, we inhibited or overexpressed *Piezo* in individual compartments of the wing disc and quantified changes in proliferation and apoptosis. When *Piezo* was knocked down in the dorsal compartment, we found a significant reduction in the number of proliferating cells (Figures 4A, 4C, and 4C′; statistics in Table S4). In comparison, overexpression of *Piezo* in the posterior compartment of the wing disc led to both compartment-specific and global increases in the number of dividing cells within the pouch (Figures 4B–4D′; statistics in Table S5). We conclude that both loss and upregulation of Piezo directly affect the regulation of cell division within the pouch. Previous studies showed that stretch activation of Piezo increases the proliferation of epithelial cells.[74] We next tested whether the pharmacological activation of Piezo by Yoda1 was sufficient to induce cell proliferation over short time periods. Sister discs (discs from the same larva) were dissected

Figure 3. Piezo regulates apical cell-cell adhesion

(A–D) *Piezo* knockdown (KD) downregulates E-Cadherin expression level. (A–B′) Optical slices along the DV axis are shown for (A) control and (B) knockdown. The arrows in (B') indicate downregulation of E-Cadherin signal. Fluorescent labels are indicated within each image. Optical slices were taken from the central region of the tissue. Scale bars, 20 μm. (C and D) Quantification of E-Cadherin intensity in the apical surface of the pouch calculated along the anterior-posterior axis for (C) control and (D) *Piezo* KD.

(E–H) *Piezo* KD downregulates apical and basal concentration levels of phospho-myosin II (pMyoII). (E–F′) Optical reslice along the DV axis of the wing disc pouch showing pMyoII expression in (E) control and (F) *Piezo* KD. Optical slices were taken from the posterior region, ~10% away from the central region of the tissue. An *Apterous*-Gal4 driver was used to drive the expression of *Piezo*^{RNAi} in the dorsal compartment of the wing disc. The arrows in (F') indicate loss in fold formation and loss of pMyoII signal. Fluorescent signals in blue, green, and red denote the patterning of nuclei, *Apterous*, and pMyoII. Scale bars, 25 μm. (G and H) Quantification of pMyoII intensity across the pouch's apical and basal compartment for (G) control and (H) *Piezo* KD. See also Figures S4–S6.

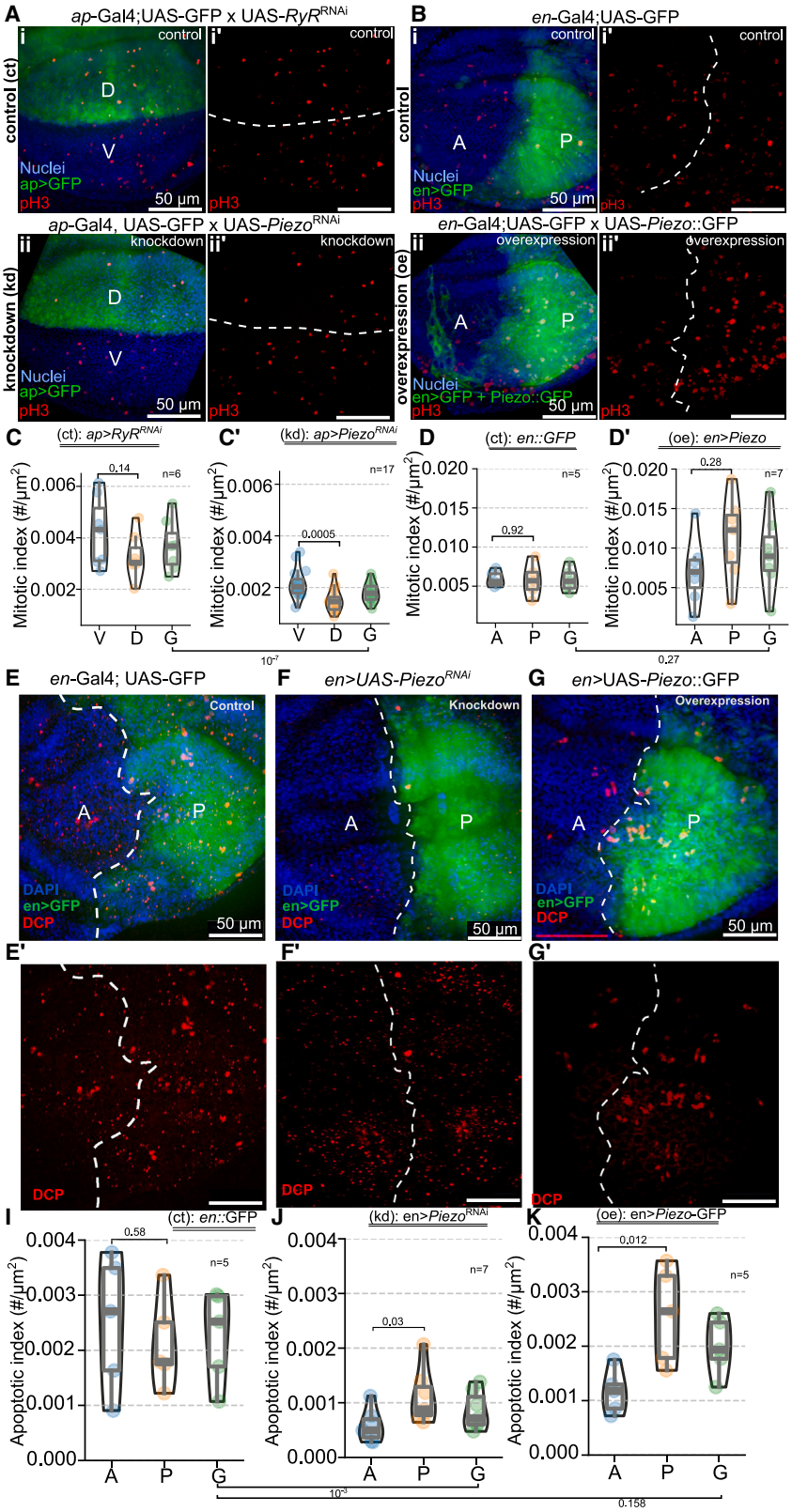

Figure 4. Piezo regulates cell proliferation and death

(A) *Piezo* was knocked down in the dorsal compartment via RNAi. Max-intensity *z*-plane projections showing expression of PH3, an indicator of proliferation, and other markers (labels indicated within the images) for the control and knockdown samples.

(B) Piezo was overexpressed in the posterior compartment. Max-intensity *z*-plane projections showing expression of PH3, an indicator of proliferation, and other markers (labels indicated within the images) for the control and Piezo overexpression samples.

(C–D′) Quantification of the mitotic index calculated as the number of dividing cells per unit square millimeter was done for both knockdown and overexpression of Piezo. Data are represented in the form of a bee-swarm plot.

(E–G′) Max-intensity *z*-plane projections showing cell death with DCP and other markers (labels indicated within the images) for the control, knockdown, and overexpression in the posterior compartment, respectively.

(I–K) Quantification of the apoptotic index defined as the number of dying cells per unit square millimeter for the indicated genotypes. Bonferroni correction was employed for statistical analysis. Data are represented in the form of a bee-swarm plot. On the x axis labels of the plots, compartments of the wing disc pouch are referred to as D, dorsal; V, ventral; A, anterior; P, posterior; and G, global (whole tissue). Scale bars, 50 µm. See also Figure S7.

and imaged for expression of an apical cell membrane marker (E-Cadherin::GFP). In agreement with the *in vivo* endpoint analysis, we observed a significant increase in cell proliferation for 60–180 min *ex vivo* on Yoda1 incubation (Figure S7; Videos S12 and S13).

In addition, *Piezo* KD in the dorsal compartment of the wing disc was stained against anti-death caspase 1 (Dcp1)[75] to mark apoptotic cells (Figure 4F). However, it should also be noted that Dcp1 may mark cells that are autophagic rather than apoptotic.[76] The antibody staining revealed a decrease in the number of cells with elevated Dcp1, indicating a decrease in apoptosis, where *Piezo* was knocked down in the posterior half of the wing disc with an *en*-Gal4 driver (Figures 4E, 4F, 4I, and 4J; statistics in Table S6). For downregulation of *Piezo* using *engrailed* (*en>Piezo*^{RNAi}), we observed a notable increase in cells positive for apoptosis on the posterior compartment compared to the anterior compartment of the same tissue (Figures 4F and 4J). We discovered that the KD of *Piezo* led to a significant global decrease in cell death across the entire wing disc pouch compared to the global values in the control group (*en>Ryr*^{RNAi}) (p value for the alternative hypothesis of unequal means is 0.0026) (Figures 4E–4G, 4I, and 4K). In the case of overexpression of *Piezo* in the posterior compartment, we observed a significant increase in apoptosis in the genetically perturbed posterior half of the tissue, i.e., apoptosis is upregulated in a compartment-specific manner (Figures 4E–4G, 4I, and 4K; statistics in Table S7).

In previous studies using MDCK cells, Piezo has been shown to regulate apical extrusion through the Rho signaling pathway to relax overcrowding.[29] Activation of Rho initiates pMyoII around the apoptotic cell, which generates the force required for its elimination from the sheet. To study the mechanism through which Piezo regulates cell death, we used a *Nubbin*-Gal4 driver to express GFP-tagged *Piezo* in the wing imaginal disc. Optical reslices along the anterior-posterior (AP) axis reveal the localization of Piezo along the cell membrane (Figures S1 and S5A). Examination of regions expressing high localization of Piezo reveals the presence of basally extruding nuclei (Figures S5B and S5C). Inspection of the localization of apoptosis with DCP-1 further supports basal extrusion, as the apoptotic cells were localized near the basal end of tissue (Figure S5C). The accumulation of pMyoII increased along the extruding nuclei, indicating a conserved mechanism of basal extrusion similar to the apical extrusion as observed within the MDCK cells.

RNAi-mediated inhibition of *Piezo* reduces the levels of two important regulators of apical-basal tension, E-Cadherin and pMyoII, consistent with the observed morphological defects. Downregulation of Piezo in the dorsal compartment reduces the levels of E-Cadherin near the apical region adjacent to the dorsal-ventral (DV) compartment boundary. In the same region, pMyoII is downregulated compared to the ventral side of the DV compartment boundary (Figures 3 and S4). Of note, we see a significantly stronger compartment-specific downregulation of E-Cadherin and pMyoII within the tissue on *Piezo* KD. This led to morphological defects during wing disc development. Further, pharmacological inhibition of Piezo via GsMTx4 also leads to a decrease in apical tension. Inhibiting *Piezo* decreases cell proliferation, while overexpression of *Piezo* increases cell proliferation. This is validated pharmacologically, where we report an increase in cell proliferation upon Piezo activation via Yoda1 (Figure S7). Moreover, we found that genetic overexpression of *Piezo* leads to an increase in cell death, while KD leads to a global decrease in apoptosis, indicating the role of Piezo in regulating tissue homeostasis (Figure 4). In sum, Piezo is a critical regulator of apical-basal tension, cell proliferation, and apoptosis during wing disc development.

Piezo controls epithelial topology

The emergence of the geometric shaping of proliferating *Drosophila* wing disc is dependent upon the multifaceted relationship between geometric constraints and biomechanical processes.[6–8] So, we next investigated if a relation exists between Piezo and epithelial topology. To study whether Piezo controls epithelial packing and cell density, we expressed UAS-*Piezo*::GFP in the dorsal compartment of the wing disc and used an E-Cadherin marker to investigate cellular adhesion, overall cell shapes, and interaction between neighbors. We found that overexpression of Piezo led to an increase in hexagonality and a decrease in cells with lower numbers of neighbors. We also observed both compartment-specific and global increases in cell area (Figures 5Aiii, 5Aiii′, and 5B, green bars; Figure S9B). Qualitatively, we show similar increases in the fraction of cells with six sides on *Piezo* overexpression. Quantification of packing topology revealed an increase in cells with lower numbers of neighbors globally in the wing disc pouch compared to control upon inhibition of *Piezo* in the dorsal compartment, but no significant changes were observed in the dorsal compartment compared to the ventral compartment (Figures 5Aii, 5Aii′, and 5B, red bars; Figure S8B). We also report a global increase in cell area upon either KD or overexpression of *Piezo* in the wing imaginal disc (Figure S9B). Based on the preliminary data, a possible explanation for the non-autonomous regulation could be changes in developmental timing upon *Piezo* expression. As cell areas in the wing disc change with time, further experiments are required to confirm the hypothesized role of Piezo in regulating developmental delay.

To validate these experimental findings and further investigate how Piezo regulates higher-order (tissue-scale) phenotypes, we incorporated additional observations on the multifaceted functional roles from a literature search that included analyses in other biological systems. Computational modeling increasingly serves critical roles in reverse-engineering biological systems.[77] From this, we utilized a computational modeling framework to generate an integrative model of Piezo's multifaceted and non-autonomous functional roles; for example, during mitosis, cells grow in size, increasing membrane tension until Piezo is activated. Following this activation, the Erk signaling pathway is triggered, facilitating the transition between G2 and M phases, initiating cell division.[6] In addition, the activation of actomyosin contractility in the cell's cortical domain during division generates this stress, which stimulates Piezo activity.[78] During proliferation, a cell is also being compressed by its neighbors until the overcrowding pressure activates Piezo, triggering the Rho signaling cascade for cell elimination and apoptosis.[74]

When *Piezo* is knocked down, the transition of cells between G2 and M phases is delayed as reduced cytosolic Ca^{2+} is not capable of activating Erk1/2.[28] This results in an increase in

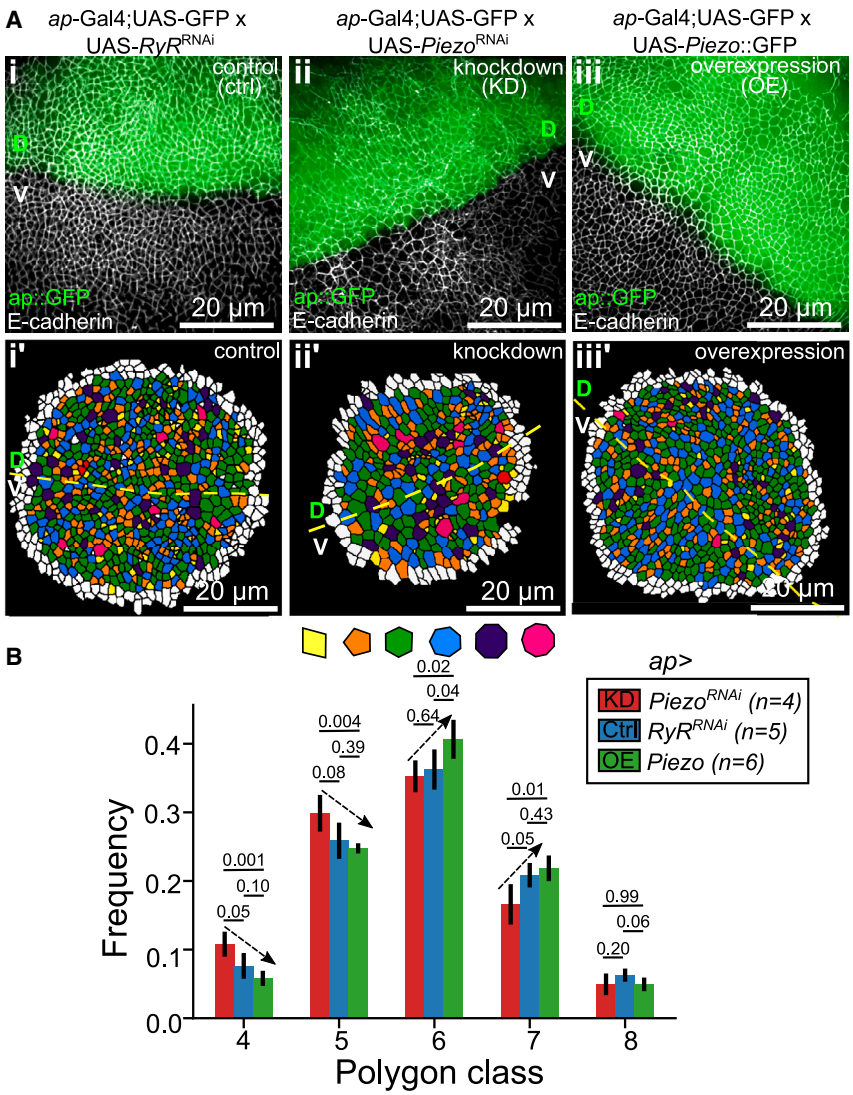

Figure 5. Piezo regulates epithelial cell topology

(A) Spatial arrangement of cells in control, *Piezo* knockdown, and *Piezo* overexpression in the dorsal compartment of the wing disc using an *ap*-Gal4 driver. Cells were color coded based on their number of neighbors. Color coding has been indicated as a key titled polygon class at the bottom. The cell counts for the epithelial packing analysis were (1) control: dorsal = 1,932, ventral = 1,621, global wing disc pouch = 3,553 cells; (2) KD: dorsal = 1,875, ventral = 1,650, global wing disc pouch = 3,525 cells; (3) OE: dorsal = 1,232, ventral = 1,124, global wing disc pouch = 2,356 cells. Scale bars, 20 μm.

(B) Quantification of the frequency of polygon class of cells within the experimental data. Error bars represent standard deviations. See also Figures S8 and S9.

cell volume, since the cells are not capable of dividing into two daughter cells. Based on these findings, our computational model posits that a loss of Piezo results in a cell's inability to sense the pressure exerted by its neighbors. As a result, an overcrowded cell will also not undergo elimination.

On the other hand, overexpression of *Piezo* can accelerate the phosphorylation of AKT and mTOR through increased cytosolic Ca^{2+} and accelerate cell-cycle progression.[33] Considering this, our computational model hypothesizes that overexpression of *Piezo* increases the hypersensitivity of the channel to changes in mechanical force required to activate the channel. Therefore, a cell will undergo extrusion and apoptosis through *Piezo* overexpression when experiencing a lower pressure threshold from its neighbor.

To test this proposed hypothesis, we implemented a vertex model following Farhadifar et al.[79,80] (Figure 6). Our vertex computational model of epithelial growth, as described in the following paragraph and in the STAR Methods section under "Quantification of epithelial packing," with a glossary of terms and parameter values in Tables S8 and S9, posits that a loss of Piezo results in a cell's inability to sense the pressure exerted by its neighbors. We first defined energy functions to account for cytoskeletal regulation within the epithelia, including line tension, perimeter contractility, and cell area elasticity (Figure 6). We also calculated the gradients in energy functions at each vertex of our model, thus characterizing the overall force experienced by each cell. Within the framework, cells experience a defined rate of growth until they reach a specific volume, as dictated by the model parameter $A_{division,cutoff}$. Division occurs when the cell area exceeds $A_{division,cutoff}$, coupled with sufficient force to activate Piezo channels ($F_{Piezo,activation}$). Similarly, eliminations and rearrangements within the epithelia are performed for cells with a size less than the $A_{elimination,cutoff}$ parameter, subjected to a force surpassing $F_{Piezo,activation}$ (Figures 6A and 6B). This assumption is based on previous known studies in which, during apoptosis, a cell is compressed by its neighbor until the pressure activates the Piezo channels, triggering the Rho signaling cascade for cell elimination.[29] We first validated the introduction of $F_{Piezo,activation}$ through simulations varying the $F_{Piezo,activation}$ parameter. As expected, our findings demonstrated that such heightened activation tension prompts cellular growth without division, resulting in a reduction in pouch size.

For case 1A, we varied the $A_{division,cutoff}$ and $A_{elimination,cutoff}$ model parameters to simulate *Piezo* genetic perturbations. To mimic increased mechanosensation upon *Piezo* overexpression, we increased $A_{cutoff,elimination}$ and decreased $A_{cutoff,division}$ in our simulations to speed up proliferative and apoptotic events (Figure 6C). As a result, we observed an increase in hexagonality, defined by the fraction of cells with six sides when proliferation and apoptosis increased together. In our experimental results,

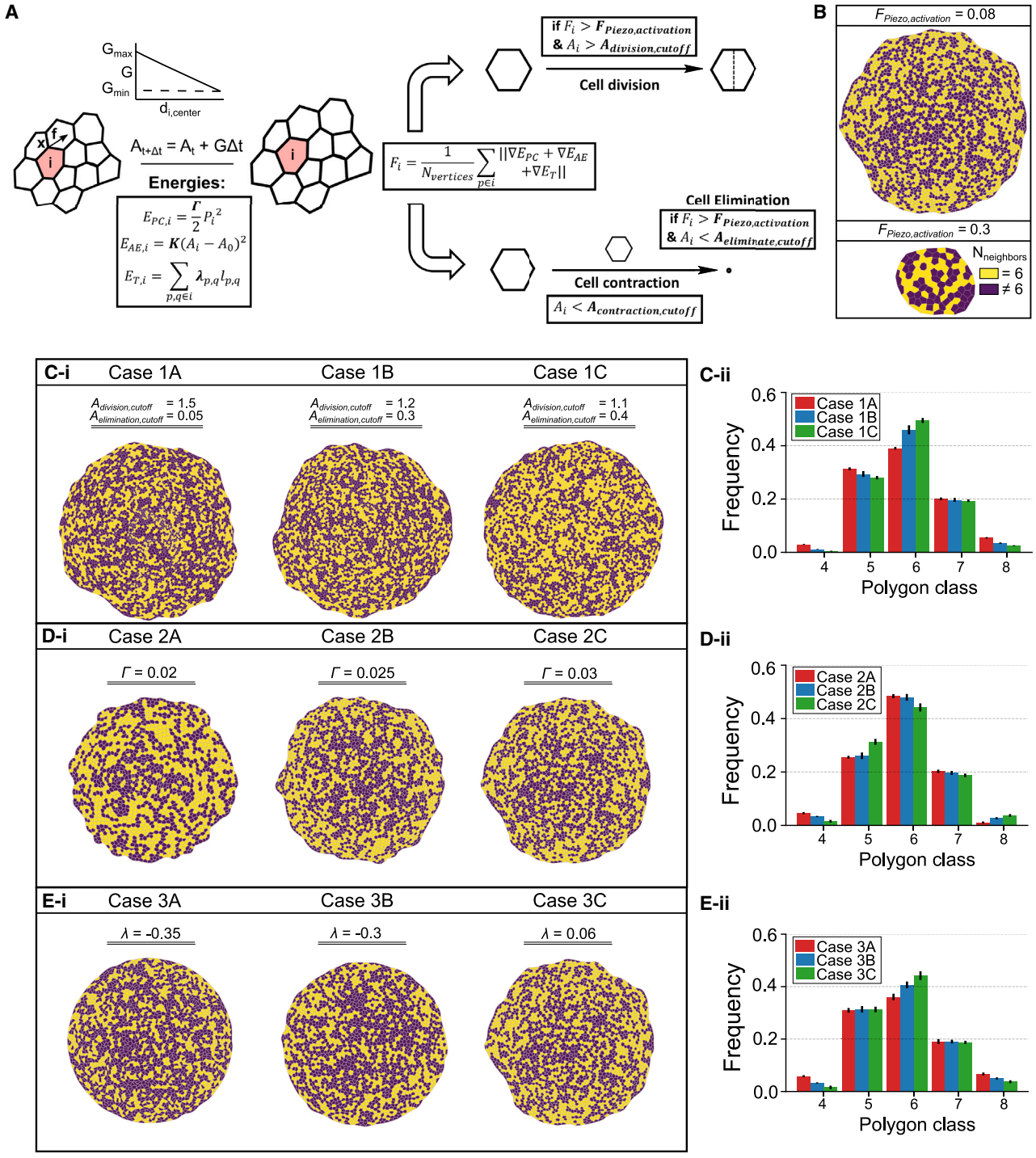

Figure 6. Activation of Piezo channels as a function of expression tunes cell topology

(A) Schematic describing the formulation for the computational model.

(B) The parameter $F_{Piezo,activation}$ value controls the functional growth of a tissue.

(C) (i) Vertex model simulations were performed by decreasing the parameter $A_{division,cutoff}$ and increasing the parameter $A_{elimination,cutoff}$. The final epithelium is visualized where the individual cells have been color coded based on their number of sides. (ii) Bar graph visualizing the distribution of polygon class for different simulation case studies performed in (i).

(D and E) (i and ii) Similar simulations were performed by increasing model parameters contractility (Γ) and line tension (λ), respectively. The yellow and purple colors signify $n = 6$ and $n \neq 6$, respectively, where n is the number of cell neighbors. See also Figure S11.

compared to hexagonality in RyR^{RNAi} expression control (0.36 ± 0.04), overexpression of *Piezo* causes an increase in hexagonality to 0.4 ± 0.04. In our computational model, where we simulate overexpression of *Piezo*, we show that fine-tuning cell division and apoptosis values can change hexagonality from 0.39 ± 0.004 to 0.49 ± 0.009. In addition to hexagonality, our model also predicts an increase in cell area as reflected by the *Piezo* overexpression analog simulation (Figure 6Cii). On the other hand, for the *Piezo* KD homolog (Figure 6C, case 1C), we also observe an increase in four- and five-sided cells, similar to our experimental data from *Piezo* KD (Figure 5B).

In the previous section, we demonstrated that the downregulation of *Piezo* reduced the expression of both pMyoII and E-Cadherin (Figure 3). Laser ablation studies further revealed that GsMtx4-treated discs cause a loss in recoil velocity (Figure S6). To study whether changes in cell proliferation are due to perturbations in cell mechanical properties, we next varied contractility (Γ) and line tension (λ) parameters within our model. A decrease in Γ increases hexagonality in packing. Strikingly, we also observed an increase in cell area (Figure 6D). Further analysis of cell area for *Piezo* KD also reveals a similar non-compartment-specific increase in normalized standard deviation in apical cell areas (Figure S9), suggesting that a partial loss of pMyoII-mediated contractility could account for the elevated cell area. Further, the decrease in contractility was similar to the increase in four-sided cells in *Piezo* KD observed in our experimental data (Figure 5B). Lastly, we varied the cell tension (λ) parameter within the model (Figure 6E). A decrease in λ reduced hexagonality in packing. Interestingly, we also observed a reduced organ growth rate (measured as the rate of change of the number of cells over time) upon increasing contractility and line tension values (Figures 6D, 6E, S11Biii, and S11Ciii). Utilizing the model, we propose that alterations in activation tension, contractility, and cell-cell adhesion collectively regulate epithelial packing and the overall size of the *Drosophila* wing disc.

Changes in λ affecting subcellular properties may be explained by E-Cadherin, as one of the cytoskeletal regulators, as it can can influence λ through cell-cell adhesion. Increased expression of E-Cadherin can effectively reduce the λ parameter.[79] Consistent with the model predictions, our results demonstrate that elevated E-Cadherin levels led by *Piezo* overexpression can lead to a reduction in cell circularity (Figures 6, S4, S4′, and S11).

Our observation of organ growth impairment when contractility and line tension were reduced implies a vital role for Piezo in organogenesis (Figures 6D and 6E). This suggests that changes in activation tension, contractility, and cell-cell adhesion together govern the arrangement of epithelial cells within the *Drosophila* wing disc.

DISCUSSION

In this study, we demonstrated that Piezo contributes to Ca^{2+} spiking frequency in the developing wing disc and directly affects the precision of size control of the adult organ. Such control over morphogenetic phenomena results from Piezo's regulation of cell-level processes, including mitosis, apoptosis, and cell topology. In a multicellular system, cytoplasmic levels of Ca^{2+} within individual cells generate dynamic patterns of Ca^{2+} throughout the entire tissue. We further report that RNAi-mediated inhibition of *Piezo* leads to severe phenotypic defects along with an overall size reduction in the adult *Drosophila* wing.[81] Overexpression of these mechanosensitive ion channels reduces the final wing size (Figure 1).

Next, we characterized how Piezo regulates the dynamics of Ca^{2+} within wing imaginal discs and found that Yoda1 activates Piezo-dependent Ca^{2+} entry in a wild-type wing disc. Activation was followed by oscillatory Ca^{2+} spikes limited to each individual cell (Figure 2). Since the intracellular Ca^{2+} was not able to diffuse to its neighbors, we hypothesized that Piezo might limit gap-junction proteins or the components of the Ca^{2+} signaling toolkit. One possibility is that the Yoda1-generated Ca^{2+} pulses are absorbed by storehouses of Ca^{2+} through pumps such as SERCA.[82] We also observed a loss in Ca^{2+} activity upon Yoda1 treatment of discs with both inhibition and overexpression of *Piezo* (Figure 2). Loss of spiking activity for discs with inhibited *Piezo* expression suggests that the observed Ca^{2+} pulses generated in the wild-type discs were specific to Piezo only. Further, the loss of Ca^{2+} activity upon overexpression, which was supplemented by loss of Ca^{2+} dynamics on 5× concentration of Yoda1 incubation (Figure S10), is consistent with the increasing flux of Ca^{2+} through ion channels first leading to a stochastic Ca^{2+} spiking response with increasing frequency, followed by a sharp decrease in oscillations due to saturation of Ca^{2+} within the cytosolic volume (Figure 2).

Stimulating discs with the Piezo agonist Yoda1 increased cell proliferation (Figure S7). Previous studies also have reported the stretch activation of Piezo channels leading to increased cell proliferation through regulation of Erk signaling.[28] There is also not much evidence about other Ca^{2+} channels interacting with one another. However, a recent study in *Drosophila* found that suppression of *Piezo-like* (*Pzl*) genes led to a slight increase in the expression of Piezo.[43] In the future, it will be interesting to test if Ca^{2+}-mediated activation of basal contractility could also be one of the triggers of cell proliferation.

Analysis of the apical surface of the epithelial cells based on the number of their neighbors provides evidence for Piezo being a regulator of overcrowding-mediated apoptosis (Figures 5 and 6). Consistent with this, we observed an increase in the number of cells with seven and eight neighbors upon inhibition of *Piezo* in the wing imaginal disc (Figure 5B). A decrease in cell density and the number of cells having nine neighbors was also observed upon overexpression of these channels. It is noteworthy that both overexpression and loss of *Piezo* were followed by an increase in apical cell size, which has not been previously reported in the literature to our knowledge. Previous studies using MDCK cells have also established the role of Piezo in relaxing overcrowding by promoting apoptosis.[74] With increasing expression of Piezo proteins within individual cells, the cells can exhibit a Ca^{2+} response at a lower pressure threshold, approximately half of what is required in wild-type cells.[83] Based on these reports and our experimental results, we developed a vertex computational model of epithelial growth to provide an integrative framework to explore the relationship between specific model parameters describing cell mechanics and their impact on the mechanical energy of the system in emergent morphological properties of the tissue, as we further discussed in the STAR

Methods section under "Quantification of epithelial packing". Our model posits that a loss of Piezo results in a cell's inability to sense the pressure exerted by its neighbors. According to the model, proliferative cells overexpressing *Piezo* could undergo a transition from G2 to M at a lower tension threshold indicated by the cell volume, leading to increased proliferative rates. In addition, for Piezo overexpression, even minimal pressure from neighboring cells could cause increase cell elimination. Piezo also regulates matrix-metalloprotease 1 (Mmp1) production in *Drosophila* midgut, leading to ECM degradation, allowing cell elimination. Ca^{2+} produced by Piezo can also activate Calpains, which facilitates ECM degradation, which supports our hypothesis.[44] Piezo also controls the elasticity of the *Drosophila* wing imaginal disc, as Mmp1 is downregulated while Collagen IV is upregulated on downregulation of Piezo.[84] These fortify our observation that Piezo is vital to tissue structural integrity, as it directly controls E-Cadherin and pMyoII (Figures 3 and S4).

In wild-type epithelia, cell size tends to correlate with the number of neighboring cells,[6,7] while apoptotic cells typically exhibit smaller sizes and fewer sides compared to non-apoptotic cells.[85,86] Therefore, reducing apoptosis would likely result in a higher prevalence of four- and five-sided cells, as they would persist rather than be eliminated from the tissue. Intriguingly, we observed that the loss of Piezo leads to an increase in four- and five-sided cells within the epithelia. Ordinarily, these four- and five-sided cells would tend to undergo apoptosis, but inhibition of *Piezo* results in a global reduction in apoptosis (Figures 4I and 4J), preventing efficient elimination of these cells and consequently increasing their abundance.

Conversely, when apoptosis is enhanced through *Piezo* overexpression, there is a corresponding decrease in the number of four- and five-sided cells. Similarly, in proliferating epithelia, hexagonal cells are predominantly present. Overexpressing *Piezo* in the dorsal compartment of the wing disc results in a tissue-wide increase of hexagonal cells, though not specifically within the dorsal compartment itself. This finding is consistent with our observation of increased proliferation upon *Piezo* overexpression. Previous studies have also noted a prevalent presence of hexagonal cells in proliferating epithelia,[7] further supporting our findings of upregulation of mitosis on *Piezo* overexpression (Figures 4B and 5B). Therefore, our findings suggest that *Piezo* expression in the dorsal compartment has systemic effects on cell topology throughout the tissue, regulating apoptosis and proliferation phenomena, ultimately contributing to the robust control of organ growth.

Piezo is also established as a force-sensing mechanotransducer.[83,87] However, the systemic and emergent roles of Piezo in morphogenesis are not fully understood. Piezo can promote apoptosis and apical extrusion to reduce cellular overcrowding, leading to the relaxation of tissues.[74] To address Piezo's role in the tissues' dependence on mechanosensitivity, we evaluated the recoil velocity of cell contraction after laser ablation and treatment with GsMTx4, a non-specific inhibitor of Piezo capable of blocking its mechanosensitive currents. When developing wing discs were treated with this inhibitor, recoil velocities were reduced, indicating a decrease in cell tension (Figure S6 and Video S16). We also demonstrated that misexpression of *Piezo* can directly affect cell area and number of neighbors, leading to overcrowded or relaxed tissues (Figures 5 and 6), suggesting Piezo's role in cellular decisions based on internal tension or pressure levels as investigated through variation of the area at which cells divide or undergo extrusion. Interestingly, our experimental investigations conducted over prolonged periods ($\geq$180 min) or with elevated concentrations of Yoda1, an activator of Piezo that is force insensitive, at 5 mM treatment or genetic overexpression of *Piezo* resulted in downregulation Ca^{2+} transients (Figure S10). Thus, upregulation of *Piezo* or force-independent activation of Piezo can lead to non-intuitive effects on Ca^{2+} signaling.

The dysregulation in cell-cell adhesion and basal contractility led by Piezo is indicative of a dysregulation in the patterning of forces as Piezo regulates key cytoskeletal regulators, such as E-Cadherin and pMyoII, which are critical for the patterning of forces within the epithelium[88,89] (Figures 3, S4, and S4′). A dysregulation in the patterning of apical, basal, and lateral forces within the wing imaginal disc can lead to organ size and shape changes.[70,71] Recently, *Piezo* KD within *Drosophila* embryos has been shown to increase heterogeneity in pMyoII cable formation post-wounding.[41] As a result, there is a faster, yet ineffective, closure of the wound. Increased phenotypic heterogeneity was also noted when activation of MEK occurred,[90] which suggests a possible shared mechanism, given Piezo's role in activating MAPK signaling,[74] to be investigated in future work.

Overall, our findings suggest that Piezo proteins play a vital role in regulating the topology of epithelial tissues by regulating cellular processes and cytoskeletal regulators in response to changes in cell size and neighboring cells, while loss of Piezo increases noise in development. Thus, Piezo forms an integral component in the complex feedback control mechanisms for tuning epithelial topology and overall organ size control.

Limitations of the study

Similar to the non-autonomous effects we observed in Piezo, other growth regulators have been identified to have tissue-level effects.[91] Possible explanations for such phenomena may include: (1) regulation of hormones or interorgan signaling impacting metabolism of the whole organ; (2) long-range impact on tissue-wide tension or pressure; or (3) regulation of metabolism through gap junctions, which allow for metabolites to be transported across tissues.[92] Further experimentation looking into the interaction between gap junctions and Piezo will provide insight into this conjecture. In addition, pharmacological inhibition of Piezo using GSMTx4 showed a decrease in cell bond tension. However, treatment of discs with the agonist Yoda1 had minimal effect on the cell bond tension (Figure S6 and Videos S14, S15, and S16). One possible explanation for this could be that Piezo expression levels act as a feedback controller to regulate the ''set-point'' tension within the tissue. Further experiments are needed, spanning multiple concentration levels and incubation periods to test this hypothesis.

STAR★METHODS

Detailed methods are provided in the online version of this paper and include the following:

- KEY RESOURCES TABLE
- RESOURCE AVAILABILITY

SUPPLEMENTAL INFORMATION

Supplemental information can be found online at https://doi.org/10.1016/j.celrep.2024.114398.

ACKNOWLEDGMENTS

Figure 2E and the graphical abstract were created with BioRender.com. This work is based upon efforts supported by the EMBRIO Institute (contract 2120200), a National Science Foundation (NSF) Biology Integration Institute. M.L., N.K., M.S.M., M.U., D.G., and J.Z. were supported in part by NIH grant R35GM124935. N.K. and J.Z. were also supported in part by NSF 2029814 and the NSF-Simons Center for Quantitative Biology Pilot program. The authors would also like to thank Pablo Cisternas Esguep, Marycruz Flores Flores, Vijay Kumar Naidu Velagala, and Dharsan Soundarrajan for their insight and helpful discussions.

AUTHOR CONTRIBUTIONS

M.S.M. and N.K. performed/replicated all experiments, analyzed the data, and wrote the manuscript. N.K. prepared the original draft and developed quantification pipelines and the vertex model. M.S.M. prepared the final manuscript and figures and performed additional experiments for revision. M.L. and M.U. performed initial experiments and analyzed the data. G.M. implemented the Ca^{2+} imaging data analysis tool. D.G. contributed to figure creation and final editing of the manuscript. T.R. contributed to experiments. J.Z. conceived, designed, analyzed, and interpreted results; supervised this study; and wrote the manuscript. All authors read and agreed to the manuscript.

DECLARATION OF INTERESTS

The authors declare that they have no competing interests.

Received: September 21, 2023
Revised: May 9, 2024
Accepted: June 10, 2024
Published: June 26, 2024

REFERENCES

1. Eder, D., Aegerter, C., and Basler, K. (2017). Forces controlling organ growth and size. Mech. Dev. *144*, 53–61. https://doi.org/10.1016/j.mod.2016.11.005.
2. Buchmann, A., Alber, M., and Zartman, J.J. (2014). Sizing it up: the mechanical feedback hypothesis of organ growth regulation. Semin. Cell Dev. Biol. *35*, 73–81. https://doi.org/10.1016/j.semcdb.2014.06.018.
3. Gómez, H.F., Dumond, M.S., Hodel, L., Vetter, R., and Iber, D. (2021). 3D cell neighbour dynamics in growing pseudostratified epithelia. Elife *10*, e68135. https://doi.org/10.7554/eLife.68135.
4. Gómez-Gálvez, P., Anbari, S., Escudero, L.M., and Buceta, J. (2021). Mechanics and self-organization in tissue development. Semin. Cell Dev. Biol. *120*, 147–159. https://doi.org/10.1016/j.semcdb.2021.07.003.
5. Lemke, S.B., and Nelson, C.M. (2021). Dynamic changes in epithelial cell packing during tissue morphogenesis. Curr. Biol. *31*, R1098–R1110. https://doi.org/10.1016/j.cub.2021.07.078.
6. Gibson, W.T., and Gibson, M.C. (2009). Chapter 4 Cell Topology, Geometry, and Morphogenesis in Proliferating Epithelia. In Current Topics in Developmental Biology Current Topics in Developmental Biology (Academic Press), pp. 87–114. https://doi.org/10.1016/S0070-2153(09)89004-2.
7. Gibson, M.C., Patel, A.B., Nagpal, R., and Perrimon, N. (2006). The emergence of geometric order in proliferating metazoan epithelia. Nature *442*, 1038–1041. https://doi.org/10.1038/nature05014.
8. Gibson, W.T., Veldhuis, J.H., Rubinstein, B., Cartwright, H.N., Perrimon, N., Brodland, G.W., Nagpal, R., and Gibson, M.C. (2011). Control of the Mitotic Cleavage Plane by Local Epithelial Topology. Cell *144*, 427–438. https://doi.org/10.1016/j.cell.2010.12.035.
9. Venables, T., Griffith, A.V., DeAraujo, A., and Petrie, H.T. (2019). Dynamic changes in epithelial cell morphology control thymic organ size during atrophy and regeneration. Nat. Commun. *10*, 4402. https://doi.org/10.1038/s41467-019-11879-2.
10. Dasgupta, A., Merkel, M., Clark, M.J., Jacob, A.E., Dawson, J.E., Manning, M.L., and Amack, J.D. (2018). Cell volume changes contribute to epithelial morphogenesis in zebrafish Kupffer's vesicle. Elife *7*, e30963. https://doi.org/10.7554/eLife.30963.
11. Brodskiy, P.A., and Zartman, J.J. (2018). Calcium as a signal integrator in developing epithelial tissues. Phys. Biol. *15*, 051001. https://doi.org/10.1088/1478-3975/aabb18.
12. Berridge, M.J., Lipp, P., and Bootman, M.D. (2000). The versatility and universality of calcium signalling. Nat. Rev. Mol. Cell Biol. *1*, 11–21. https://doi.org/10.1038/35036035.
13. Pan, Y., Heemskerk, I., Ibar, C., Shraiman, B.I., and Irvine, K.D. (2016). Differential growth triggers mechanical feedback that elevates Hippo signaling. Proc. Natl. Acad. Sci. USA *113*, E6974–E6983. https://doi.org/10.1073/pnas.1615012113.
14. Ostalé, C.M., Vega-Cuesta, P., González, T., López-Varea, A., and de Celis, J.F. (2023). RNAi screen in the Drosophila wing of genes encoding proteins related to cytoskeleton organization and cell division. Dev. Biol. *498*, 61–76. https://doi.org/10.1016/j.ydbio.2023.03.010.
15. LeGoff, L., and Lecuit, T. (2015). Mechanical Forces and Growth in Animal Tissues. Cold Spring Harb. Perspect. Biol. *8*, a019232. https://doi.org/10.1101/cshperspect.a019232.
16. Chugh, M., Munjal, A., and Megason, S.G. (2022). Hydrostatic pressure as a driver of cell and tissue morphogenesis. Semin. Cell Dev. Biol. *131*, 134–145. https://doi.org/10.1016/j.semcdb.2022.04.021.
17. Roy Choudhury, A., Großhans, J., and Kong, D. (2021). Ion Channels in Epithelial Dynamics and Morphogenesis. Cells *10*, 2280. https://doi.org/10.3390/cells10092280.
18. Duchemin, A.-L., Vignes, H., and Vermot, J. (2019). Mechanically activated piezo channels modulate outflow tract valve development through the Yap1 and Klf2-Notch signaling axis. Elife *8*, e44706. https://doi.org/10.7554/eLife.44706.
19. Ingber, D.E. (2006). Cellular mechanotransduction: putting all the pieces together again. FASEB J. Off. Publ. Fed. Am. Soc. Exp. Biol. *20*, 811–827. https://doi.org/10.1096/fj.05-5424rev.
20. Coste, B., Mathur, J., Schmidt, M., Earley, T.J., Ranade, S., Petrus, M.J., Dubin, A.E., and Patapoutian, A. (2010). Piezo1 and Piezo2 are essential components of distinct mechanically activated cation channels. Science *330*, 55–60. https://doi.org/10.1126/science.1193270.
21. Chesler, A.T., and Szczot, M. (2018). Portraits of a pressure sensor. Elife *7*, e34396. https://doi.org/10.7554/eLife.34396.

22. Guo, Y.R., and MacKinnon, R. (2017). Structure-based membrane dome mechanism for Piezo mechanosensitivity. Elife *6*, e33660. https://doi.org/10.7554/eLife.33660.

23. Beech, D.J., and Kalli, A.C. (2019). Force Sensing by Piezo Channels in Cardiovascular Health and Disease. Arterioscler. Thromb. Vasc. Biol. *39*, 2228–2239. https://doi.org/10.1161/ATVBAHA.119.313348.

24. Aglialoro, F., Abay, A., Yagci, N., Rab, M.A.E., Kaestner, L., van Wijk, R., von Lindern, M., and van den Akker, E. (2021). Mechanical Stress Induces Ca2+-Dependent Signal Transduction in Erythroblasts and Modulates Erythropoiesis. Int. J. Mol. Sci. *22*, 955. https://doi.org/10.3390/ijms22020955.

25. Wang, Y., Zhang, Z., Yang, Q., Cao, Y., Dong, Y., Bi, Y., and Liu, G. (2022). Immunoregulatory Role of the Mechanosensitive Ion Channel Piezo1 in Inflammation and Cancer. Molecules *28*, 213. https://doi.org/10.3390/molecules28010213.

26. Liu, S., Xu, X., Fang, Z., Ning, Y., Deng, B., Pan, X., He, Y., Yang, Z., Huang, K., and Li, J. (2021). Piezo1 impairs hepatocellular tumor growth via deregulation of the MAPK-mediated YAP signaling pathway. Cell Calcium *95*, 102367. https://doi.org/10.1016/j.ceca.2021.102367.

27. Zhong, M., Komarova, Y., Rehman, J., and Malik, A.B. (2018). Mechanosensing Piezo channels in tissue homeostasis including their role in lungs. Pulm. Circ. *8*, 2045894018767393. https://doi.org/10.1177/2045894018767393.

28. Piddini, E. (2017). Epithelial Homeostasis: A Piezo of the Puzzle. Curr. Biol. *27*, R232–R234. https://doi.org/10.1016/j.cub.2017.02.002.

29. Eisenhoffer, G.T., Loftus, P.D., Yoshigi, M., Otsuna, H., Chien, C.-B., Morcos, P.A., and Rosenblatt, J. (2012). Crowding induces live cell extrusion to maintain homeostatic cell numbers in epithelia. Nature *484*, 546–549. https://doi.org/10.1038/nature10999.

30. De Felice, D., and Alaimo, A. (2020). Mechanosensitive Piezo Channels in Cancer: Focus on altered Calcium Signaling in Cancer Cells and in Tumor Progression. Cancers *12*, 1780. https://doi.org/10.3390/cancers12071780.

31. Chen, X., Wanggou, S., Bodalia, A., Zhu, M., Dong, W., Fan, J.J., Yin, W.C., Min, H.-K., Hu, M., Draghici, D., et al. (2018). A Feedforward Mechanism Mediated by Mechanosensitive Ion Channel PIEZO1 and Tissue Mechanics Promotes Glioma Aggression. Neuron *100*, 799–815.e7. https://doi.org/10.1016/j.neuron.2018.09.046.

32. Wang, J., Jiang, J., Yang, X., Zhou, G., Wang, L., and Xiao, B. (2022). Tethering Piezo channels to the actin cytoskeleton for mechanogating via the cadherin-β-catenin mechanotransduction complex. Cell Rep. *38*, 110342. https://doi.org/10.1016/j.celrep.2022.110342.

33. Pardo-Pastor, C., Rubio-Moscardo, F., Vogel-González, M., Serra, S.A., Afthinos, A., Mrkonjic, S., Destaing, O., Abenza, J.F., Fernández-Fernández, J.M., Trepat, X., et al. (2018). Piezo2 channel regulates RhoA and actin cytoskeleton to promote cell mechanobiological responses. Proc. Natl. Acad. Sci. USA *115*, 1925–1930. https://doi.org/10.1073/pnas.1718177115.

34. Nie, X., and Chung, M.-K. (2022). Piezo channels for skeletal development and homeostasis: Insights from mouse genetic models. Differentiation. *126*, 10–15. https://doi.org/10.1016/j.diff.2022.06.001.

35. Koser, D.E., Thompson, A.J., Foster, S.K., Dwivedy, A., Pillai, E.K., Sheridan, G.K., Svoboda, H., Viana, M., Costa, L.d.F., Guck, J., et al. (2016). Mechanosensing is critical for axon growth in the developing brain. Nat. Neurosci. *19*, 1592–1598. https://doi.org/10.1038/nn.4394.

36. Srivastava, N., Traynor, D., Piel, M., Kabla, A.J., and Kay, R.R. (2020). Pressure sensing through Piezo channels controls whether cells migrate with blebs or pseudopods. Proc. Natl. Acad. Sci. USA *117*, 2506–2512. https://doi.org/10.1073/pnas.1905730117.

37. Bernareggi, A., Bosutti, A., Massaria, G., Giniatullin, R., Malm, T., Sciancalepore, M., and Lorenzon, P. (2022). The State of the Art of Piezo1 Channels in Skeletal Muscle Regeneration. Int. J. Mol. Sci. *23*, 6616. https://doi.org/10.3390/ijms23126616.

38. Sugimoto, A., Miyazaki, A., Kawarabayashi, K., Shono, M., Akazawa, Y., Hasegawa, T., Ueda-Yamaguchi, K., Kitamura, T., Yoshizaki, K., Fukumoto, S., and Iwamoto, T. (2017). Piezo type mechanosensitive ion channel component 1 functions as a regulator of the cell fate determination of mesenchymal stem cells. Sci. Rep. *7*, 17696. https://doi.org/10.1038/s41598-017-18089-0.

39. Ranade, S.S., Qiu, Z., Woo, S.-H., Hur, S.S., Murthy, S.E., Cahalan, S.M., Xu, J., Mathur, J., Bandell, M., Coste, B., et al. (2014). Piezo1, a mechanically activated ion channel, is required for vascular development in mice. Proc. Natl. Acad. Sci. USA *111*, 10347–10352. https://doi.org/10.1073/pnas.1409233111.

40. He, L., Si, G., Huang, J., Samuel, A.D.T., and Perrimon, N. (2018). Mechanical regulation of stem-cell differentiation by the stretch-activated Piezo channel. Nature *555*, 103–106. https://doi.org/10.1038/nature25744.

41. Zechini, L., Amato, C., Scopelliti, A., and Wood, W. (2022). Piezo acts as a molecular brake on wound closure to ensure effective inflammation and maintenance of epithelial integrity. Curr. Biol. *32*, 3584–3592.e4. https://doi.org/10.1016/j.cub.2022.06.041.

42. Song, Y., Li, D., Farrelly, O., Miles, L., Li, F., Kim, S.E., Lo, T.Y., Wang, F., Li, T., Thompson-Peer, K.L., et al. (2019). The Mechanosensitive Ion Channel Piezo Inhibits Axon Regeneration. Neuron *102*, 373–389.e6. https://doi.org/10.1016/j.neuron.2019.01.050.

43. Hu, Y., Wang, Z., Liu, T., and Zhang, W. (2019). Piezo-like Gene Regulates Locomotion in Drosophila Larvae. Cell Rep. *26*, 1369–1377.e4. https://doi.org/10.1016/j.celrep.2019.01.055.

44. Lee, J., Cabrera, A.J.H., Nguyen, C.M.T., and Kwon, Y.V. (2020). Dissemination of RasV12-transformed cells requires the mechanosensitive channel Piezo. Nat. Commun. *11*, 3568. https://doi.org/10.1038/s41467-020-17341-y.

45. Soundarrajan, D.K., Huizar, F.J., Paravitorghabeh, R., Robinett, T., and Zartman, J.J. (2021). From spikes to intercellular waves: Tuning intercellular calcium signaling dynamics modulates organ size control. PLoS Comput. Biol. *17*, e1009543. https://doi.org/10.1371/journal.pcbi.1009543.

46. Wu, Q., Kumar, N., Velagala, V., and Zartman, J.J. (2019). Tools to reverse-engineer multicellular systems: case studies using the fruit fly. J. Biol. Eng. *13*, 33. https://doi.org/10.1186/s13036-019-0161-8.

47. Kim, S.E., Coste, B., Chadha, A., Cook, B., and Patapoutian, A. (2012). The role of Drosophila Piezo in mechanical nociception. Nature *483*, 209–212. https://doi.org/10.1038/nature10801.

48. Li, J., Hou, B., Tumova, S., Muraki, K., Bruns, A., Ludlow, M.J., Sedo, A., Hyman, A.J., McKeown, L., Young, R.S., et al. (2014). Piezo1 integration of vascular architecture with physiological force. Nature *515*, 279–282. https://doi.org/10.1038/nature13701.

49. Szczot, M., Nickolls, A.R., Lam, R.M., and Chesler, A.T. (2021). The Form and Function of PIEZO2. Annu. Rev. Biochem. *90*, 507–534. https://doi.org/10.1146/annurev-biochem-081720-023244.

50. Brodskiy, P.A., Wu, Q., Soundarrajan, D.K., Huizar, F.J., Chen, J., Liang, P., Narciso, C., Levis, M.K., Arredondo-Walsh, N., Chen, D.Z., and Zartman, J.J. (2019). Decoding Calcium Signaling Dynamics during Drosophila Wing Disc Development. Biophys. J. *116*, 725–740. https://doi.org/10.1016/j.bpj.2019.01.007.

51. Narciso, C., Wu, Q., Brodskiy, P., Garston, G., Baker, R., Fletcher, A., and Zartman, J. (2015). Patterning of wound-induced intercellular Ca2+ flashes in a developing epithelium. Phys. Biol. *12*, 056005. https://doi.org/10.1088/1478-3975/12/5/056005.

52. Graveley, B.R., Brooks, A.N., Carlson, J.W., Duff, M.O., Landolin, J.M., Yang, L., Artieri, C.G., van Baren, M.J., Boley, N., Booth, B.W., et al. (2011). The developmental transcriptome of Drosophila melanogaster. Nature *471*, 473–479. https://doi.org/10.1038/nature09715.

53. Naito, Y., Yamada, T., Matsumiya, T., Ui-Tei, K., Saigo, K., and Morishita, S. (2005). dsCheck: highly sensitive off-target search software for

double-stranded RNA-mediated RNA interference. Nucleic Acids Res. *33*, W589–W591. https://doi.org/10.1093/nar/gki419.

54. Oh, S.M., Jeong, K., Seo, J.T., and Moon, S.J. (2021). Multisensory interactions regulate feeding behavior in Drosophila. Proc. Natl. Acad. Sci. USA *118*, e2004523118. https://doi.org/10.1073/pnas.2004523118.
55. Wang, P., Jia, Y., Liu, T., Jan, Y.-N., and Zhang, W. (2020). Visceral Mechano-sensing Neurons Control Drosophila Feeding by Using Piezo as a Sensor. Neuron *108*, 640–650.e4. https://doi.org/10.1016/j.neuron.2020.08.017.
56. Lopez-Bellido, R., Puig, S., Huang, P.J., Tsai, C.-R., Turner, H.N., Galko, M.J., and Gutstein, H.B. (2019). Growth Factor Signaling Regulates Mechanical Nociception in Flies and Vertebrates. J. Neurosci. *39*, 6012–6030. https://doi.org/10.1523/JNEUROSCI.2950-18.2019.
57. Martinac, B. (2012). Mechanosensitive ion channels: an evolutionary and scientific tour de force in mechanobiology. Channels *6*, 211–213. https://doi.org/10.4161/chan.22047.
58. Stewart, T.A., and Davis, F.M. (2019). An element for development: Calcium signaling in mammalian reproduction and development. Biochim. Biophys. Acta. Mol. Cell Res. *1866*, 1230–1238. https://doi.org/10.1016/j.bbamcr.2019.02.016.
59. Botello-Smith, W.M., Jiang, W., Zhang, H., Ozkan, A.D., Lin, Y.-C., Pham, C.N., Lacroix, J.J., and Luo, Y. (2019). A mechanism for the activation of the mechanosensitive Piezo1 channel by the small molecule Yoda1. Nat. Commun. *10*, 4503. https://doi.org/10.1038/s41467-019-12501-1.
60. Yang, S., Miao, X., Arnold, S., Li, B., Ly, A.T., Wang, H., Wang, M., Guo, X., Pathak, M.M., Zhao, W., et al. (2022). Membrane curvature governs the distribution of Piezo1 in live cells. Nat. Commun. *13*, 7467. https://doi.org/10.1038/s41467-022-35034-6.
61. Chen, T.-W., Wardill, T.J., Sun, Y., Pulver, S.R., Renninger, S.L., Baohan, A., Schreiter, E.R., Kerr, R.A., Orger, M.B., Jayaraman, V., et al. (2013). Ultrasensitive fluorescent proteins for imaging neuronal activity. Nature *499*, 295–300. https://doi.org/10.1038/nature12354.
62. Dupont, G., and Goldbeter, A. (1993). One-pool model for Ca^{2+} oscillations involving Ca2+ and inositol 1,4,5-trisphosphate as co-agonists for Ca2+ release. Cell Calcium *14*, 311–322. https://doi.org/10.1016/0143-4160(93)90052-8.
63. modENCODE Consortium; Roy, S., Ernst, J., Kharchenko, P.V., Kheradpour, P., Negre, N., Eaton, M.L., Landolin, J.M., Bristow, C.A., Ma, L., et al. (2010). Identification of Functional Elements and Regulatory Circuits by Drosophila modENCODE. Science *330*, 1787–1797. https://doi.org/10.1126/science.1198374.
64. Ma, H.-T., Patterson, R.L., van Rossum, D.B., Birnbaumer, L., Mikoshiba, K., and Gill, D.L. (2000). Requirement of the Inositol Trisphosphate Receptor for Activation of Store-Operated Ca2+ Channels. Science *287*, 1647–1651. https://doi.org/10.1126/science.287.5458.1647.
65. Wang, X., Cheng, G., Miao, Y., Qiu, F., Bai, L., Gao, Z., Huang, Y., Dong, L., Niu, X., Wang, X., et al. (2021). Piezo type mechanosensitive ion channel component 1 facilitates gastric cancer omentum metastasis. J. Cell Mol. Med. *25*, 2238–2253. https://doi.org/10.1111/jcmm.16217.
66. Cachoux, V.M.L., Balakireva, M., Gracia, M., Bosveld, F., López-Gay, J.M., Maugarny, A., Gaugué, I., di Pietro, F., Rigaud, S.U., Noiret, L., et al. (2023). Epithelial apoptotic pattern emerges from global and local regulation by cell apical area. Curr. Biol. *33*, 4807–4826.e6. https://doi.org/10.1016/j.cub.2023.09.049.
67. Wodarz, A., Stewart, D.B., Nelson, W.J., and Nusse, R. (2006). Wingless signaling modulates cadherin-mediated cell adhesion in Drosophila imaginal disc cells. J. Cell Sci. *119*, 2425–2434. https://doi.org/10.1242/jcs.02973.
68. Gumbiner, B.M. (1996). Cell Adhesion: The Molecular Basis of Tissue Architecture and Morphogenesis. Cell *84*, 345–357. https://doi.org/10.1016/S0092-8674(00)81279-9.
69. Liang, X., Weberling, A., Hii, C.Y., Zernicka-Goetz, M., and Buckley, C.E. (2022). E-cadherin mediates apical membrane initiation site localisation during de novo polarisation of epithelial cavities. EMBO J. *41*, e111021. https://doi.org/10.15252/embj.2022111021.
70. Nematbakhsh, A., Levis, M., Kumar, N., Chen, W., Zartman, J.J., and Alber, M. (2020). Epithelial organ shape is generated by patterned actomyosin contractility and maintained by the extracellular matrix. PLoS Comput. Biol. *16*, e1008105. https://doi.org/10.1371/journal.pcbi.1008105.
71. Kumar, N., Rangel Ambriz, J., Tsai, K., Mim, M.S., Flores-Flores, M., Chen, W., Zartman, J.J., and Alber, M. (2024). Balancing competing effects of tissue growth and cytoskeletal regulation during Drosophila wing disc development. Nat. Commun. *15*, 2477. https://doi.org/10.1038/s41467-024-46698-7.
72. Harmansa, S., Erlich, A., Eloy, C., Zurlo, G., and Lecuit, T. (2023). Growth anisotropy of the extracellular matrix shapes a developing organ. Nat. Commun. *14*, 1220. https://doi.org/10.1038/s41467-023-36739-y.
73. Bae, C., Sachs, F., and Gottlieb, P.A. (2011). The mechanosensitive ion channel Piezo1 is inhibited by the peptide GsMTx4. Biochemistry *50*, 6295–6300. https://doi.org/10.1021/bi200770q.
74. Gudipaty, S.A., Lindblom, J., Loftus, P.D., Redd, M.J., Edes, K., Davey, C.F., Krishnegowda, V., and Rosenblatt, J. (2017). Mechanical stretch triggers rapid epithelial cell division through Piezo1. Nature *543*, 118–121. https://doi.org/10.1038/nature21407.
75. Song, Z., McCall, K., and Steller, H. (1997). DCP-1, a Drosophila Cell Death Protease Essential for Development. Science *275*, 536–540. https://doi.org/10.1126/science.275.5299.536.
76. DeVorkin, L., Go, N.E., Hou, Y.-C.C., Moradian, A., Morin, G.B., and Gorski, S.M. (2014). The Drosophila effector caspase Dcp-1 regulates mitochondrial dynamics and autophagic flux via SesB. J. Cell Biol. *205*, 477–492. https://doi.org/10.1083/jcb.201303144.
77. Brodland, G.W. (2015). How computational models can help unlock biological systems. Semin. Cell Dev. Biol. *47–48*, 62–73. https://doi.org/10.1016/j.semcdb.2015.07.001.
78. Meyer, E.J., Ikmi, A., and Gibson, M.C. (2011). Interkinetic nuclear migration is a broadly conserved feature of cell division in pseudostratified epithelia. Curr. Biol. *21*, 485–491. https://doi.org/10.1016/j.cub.2011.02.002.
79. Farhadifar, R., Röper, J.-C., Aigouy, B., Eaton, S., and Jülicher, F. (2007). The influence of cell mechanics, cell-cell interactions, and proliferation on epithelial packing. Curr. Biol. *17*, 2095–2104. https://doi.org/10.1016/j.cub.2007.11.049.
80. Fletcher, A.G., Cooper, F., and Baker, R.E. (2017). Mechanocellular models of epithelial morphogenesis. Philos. Trans. R. Soc. Lond. B Biol. Sci. *372*, 20150519. https://doi.org/10.1098/rstb.2015.0519.
81. Kumar, N., Huizar, F.J., Farfán-Pira, K.J., Brodskiy, P.A., Soundarrajan, D.K., Nahmad, M., and Zartman, J.J. (2022). MAPPER: An Open-Source, High-Dimensional Image Analysis Pipeline Unmasks Differential Regulation of Drosophila Wing Features. Front. Genet. *13*, 869719. https://doi.org/10.3389/fgene.2022.869719.
82. Zhang, T., Chi, S., Jiang, F., Zhao, Q., and Xiao, B. (2017). A protein interaction mechanism for suppressing the mechanosensitive Piezo channels. Nat. Commun. *8*, 1797. https://doi.org/10.1038/s41467-017-01712-z.
83. Coste, B., Xiao, B., Santos, J.S., Syeda, R., Grandl, J., Spencer, K.S., Kim, S.E., Schmidt, M., Mathur, J., Dubin, A.E., et al. (2012). Piezo proteins are pore-forming subunits of mechanically activated channels. Nature *483*, 176–181. https://doi.org/10.1038/nature10812.
84. Kumar, N., Mim, M.S., Dowling, A., and Zartman, J.J. (2024). Reverse engineering morphogenesis through Bayesian optimization of physics-based models. Npj Syst. Biol. Appl. *10*, 49. https://doi.org/10.1038/s41540-024-00375-z.
85. Nematbakhsh, A., Sun, W., Brodskiy, P.A., Amiri, A., Narciso, C., Xu, Z., Zartman, J.J., and Alber, M. (2017). Multi-scale computational study of the mechanical regulation of cell mitotic rounding in epithelia. PLoS Comput. Biol. *13*, e1005533. https://doi.org/10.1371/journal.pcbi.1005533.

86. Tsuboi, A., Ohsawa, S., Umetsu, D., Sando, Y., Kuranaga, E., Igaki, T., and Fujimoto, K. (2018). Competition for Space Is Controlled by Apoptosis-Induced Change of Local Epithelial Topology. Curr. Biol. *28*, 2115–2128.e5. https://doi.org/10.1016/j.cub.2018.05.029.

87. Jiang, Y., Yang, X., Jiang, J., and Xiao, B. (2021). Structural Designs and Mechanogating Mechanisms of the Mechanosensitive Piezo Channels. Trends Biochem. Sci. *46*, 472–488. https://doi.org/10.1016/j.tibs.2021.01.008.

88. Cabrera, A.J.H., Gumbiner, B.M., and Kwon, Y.V. (2021). The roles of distinct Ca2+ signaling mediated by Piezo and inositol triphosphate receptor (IP3R) in the remodeling of E-cadherin during cell dissemination. Preprint at bioRxiv. https://doi.org/10.1101/2021.11.10.467957.

89. Heer, N.C., Miller, P.W., Chanet, S., Stoop, N., Dunkel, J., and Martin, A.C. (2017). Actomyosin-based tissue folding requires a multicellular myosin gradient. Dev. Camb. Engl. *144*, 1876–1886. https://doi.org/10.1242/dev.146761.

90. Marmion, R.A., Simpkins, A.G., Barrett, L.A., Denberg, D.W., Zusman, S., Schottenfeld-Roames, J., Schüpbach, T., and Shvartsman, S.Y. (2023). Stochastic phenotypes in RAS-dependent developmental diseases. Curr. Biol. *33*, 807–816.e4. https://doi.org/10.1016/j.cub.2023.01.008.

91. Galloni, M., and Edgar, B.A. (1999). Cell-autonomous and non-autonomous growth-defective mutants of Drosophila melanogaster. Development *126*, 2365–2375. https://doi.org/10.1242/dev.126.11.2365.

92. Boumard, B., Meur, G.L., Maalouf, T., El-Hajj, M., Bauer, R., and Bardin, A.J. (2023). Nucleotide sharing through gap junctions buffers replication stress. Preprint at bioRxiv. https://doi.org/10.1101/2023.08.15.553366.

93. Schindelin, J., Arganda-Carreras, I., Frise, E., Kaynig, V., Longair, M., Pietzsch, T., Preibisch, S., Rueden, C., Saalfeld, S., Schmid, B., et al. (2012). Fiji: an open-source platform for biological-image analysis. Nat. Methods *9*, 676–682. https://doi.org/10.1038/nmeth.2019.

94. Levis, M., Kumar, N., Apakian, E., Moreno, C., Hernandez, U., Olivares, A., Ontiveros, F., and Zartman, J.J. (2019). Microfluidics on the fly: Inexpensive rapid fabrication of thermally laminated microfluidic devices for live imaging and multimodal perturbations of multicellular systems. Biomicrofluidics *13*, 024111. https://doi.org/10.1063/1.5086671.

95. Dye, N.A., Popović, M., Spannl, S., Etournay, R., Kainmüller, D., Ghosh, S., Myers, E.W., Jülicher, F., and Eaton, S. (2017). Cell dynamics underlying oriented growth of the Drosophila wing imaginal disc. Dev. Camb. Engl. *144*, 4406–4421. https://doi.org/10.1242/dev.155069.

96. Huebner, R.J., Malmi-Kakkada, A.N., Sarıkaya, S., Weng, S., Thirumalai, D., and Wallingford, J.B. (2021). Mechanical heterogeneity along single cell-cell junctions is driven by lateral clustering of cadherins during vertebrate axis elongation. Elife *10*, e65390. https://doi.org/10.7554/eLife.65390.

97. Liang, X., Michael, M., and Gomez, G.A. (2016). Measurement of Mechanical Tension at Cell-cell Junctions Using Two-photon Laser Ablation. Bio. Protoc. *6*, e2068. https://doi.org/10.21769/BioProtoc.2068.

98. Giovannucci, A., Friedrich, J., Gunn, P., Kalfon, J., Brown, B.L., Koay, S.A., Taxidis, J., Najafi, F., Gauthier, J.L., Zhou, P., et al. (2019). CaImAn an open source tool for scalable calcium imaging data analysis. Elife *8*, e38173. https://doi.org/10.7554/eLife.38173.

99. Pnevmatikakis, E.A. (2019). Analysis pipelines for calcium imaging data. Curr. Opin. Neurobiol. *55*, 15–21. https://doi.org/10.1016/j.conb.2018.11.004.

100. Virtanen, P., Gommers, R., Oliphant, T.E., Haberland, M., Reddy, T., Cournapeau, D., Burovski, E., Peterson, P., Weckesser, W., Bright, J., et al. (2020). SciPy 1.0: fundamental algorithms for scientific computing in Python. Nat. Methods *17*, 261–272. https://doi.org/10.1038/s41592-019-0686-2.

101. Hunter, J.D. (2007). Matplotlib: A 2D Graphics Environment. Comput. Sci. Eng. *9*, 90–95. https://doi.org/10.1109/MCSE.2007.55.

102. Seabold, S., and Perktold, J. (2010). Statsmodels: Econometric and Statistical Modeling with Python. Proceedings of the Python in Science Conference. p. 92–96. https://doi.org/10.25080/Majora-92bf1922-011.

103. Pedregosa, F., Varoquaux, G., Gramfort, A., Michel, V., Thirion, B., Grisel, O., Blondel, M., Prettenhofer, P., Weiss, R., Dubourg, V., et al. (2011). Scikit-learn: Machine Learning in Python. J. Mach. Learn. Res. *12*, 2825–2830.

104. Weigert, M., Schmidt, U., Boothe, T., Müller, A., Dibrov, A., Jain, A., Wilhelm, B., Schmidt, D., Broaddus, C., Culley, S., et al. (2018). Content-aware image restoration: pushing the limits of fluorescence microscopy. Nat. Methods *15*, 1090–1097. https://doi.org/10.1038/s41592-018-0216-7.

105. Aigouy, B., Cortes, C., Liu, S., and Prud'Homme, B. (2020). EPySeg: a coding-free solution for automated segmentation of epithelia using deep learning. Development *147*, dev194589. https://doi.org/10.1242/dev.194589.

106. LeGoff, L., Rouault, H., and Lecuit, T. (2013). A global pattern of mechanical stress polarizes cell divisions and cell shape in the growing Drosophila wing disc. Development *140*, 4051–4059. https://doi.org/10.1242/dev.090878.

107. Theis, S., Suzanne, M., and Gay, G. (2021). Tyssue: an epithelium simulation library. J. Open Source Softw. *6*, 2973. https://doi.org/10.21105/joss.02973.

108. Mao, Y., Tournier, A.L., Hoppe, A., Kester, L., Thompson, B.J., and Tapon, N. (2013). Differential proliferation rates generate patterns of mechanical tension that orient tissue growth. EMBO J. *32*, 2790–2803. https://doi.org/10.1038/emboj.2013.197.

109. Monier, B., Gettings, M., Gay, G., Mangeat, T., Schott, S., Guarner, A., and Suzanne, M. (2015). Apico-basal forces exerted by apoptotic cells drive epithelium folding. Nature *518*, 245–248. https://doi.org/10.1038/nature14152.

110. Mishra, P., Singh, U., Pandey, C.M., Mishra, P., and Pandey, G. (2019). Application of Student's t-test, Analysis of Variance, and Covariance. Ann. Card Anaesth. *22*, 407–411. https://doi.org/10.4103/aca.ACA_94_19.

111. Arsham, H., and Lovric, M. (2011). Bartlett's Test. In International Encyclopedia of Statistical Science, M. Lovric, ed. (Springer), pp. 87–88. https://doi.org/10.1007/978-3-642-04898-2_132.

112. Cohen, J. (1988). Statistical Power Analysis for the Behavioral Sciences, 2nd ed. (Routledge). https://doi.org/10.4324/9780203771587.

STAR★METHODS

KEY RESOURCES TABLE

REAGENT or RESOURCE	SOURCE	IDENTIFIER
Antibodies		
P-Histone H3 (PH3)	Cell Signaling Technology	Cat#9701; RRID: AB_331535
Dcp-1	Cell Signaling Technology	Cat#9578 RRID: AB_2721060
E-Cadherin (DCAD2)	UIOWA/DSHB	Cat#DCAD2; RRID: AB_528120
Phospho-Myosin Light Chain 2 (Ser19) Antibody #3671 (pMyoII)	Cell Signaling Technology	Cat# 3675, RRID:AB_2250969
Goat anti-Mouse IgG Alexa Fluor™ 568	Thermo Fisher Scientific	Cat#A-11031; RRID: AB_144696
Goat anti-mouse IgG Alexa Fluor™ 647	Thermo FisherScientific	Cat#A-21235; RRID: AB_2535804
Chemicals, peptides, and recombinant proteins		
Paraformaldehyde	Thermo Fisher Scientific	Cat# J19943.K2
Triton-X 100	Thermo Fisher Scientific	Cat# BP151-500
PBS	Sigma-Aldrich	Cat# P5368
Normal goat serum	Thermo Fisher Scientific	Cat# 50197Z
Grace's Insect Medium	Sigma-Aldrich	Prod# G9771; MDL# MFCD00147059
Bis Tris	Sigma-Aldrich	Prod# B4429; CAS# 6976-37-0
Fetal bovine serum	Sigma-Aldrich	Prod# F2442; MDL# MFCD00132239
20-Hydroxyecdysone	Sigma-Aldrich	Prod# H5142; CAS# 5289-74-7
Penicillin and streptomycin	Sigma-Aldrich	Prod# P4333
Yoda1	Sigma Aldrich	Prod# SML1558; CAS# 448947-81-7
DAPI	Sigma Aldrich	Prod# D9542; CAS# 28718-90-3
2-APB	Sigma-Aldrich	Prod# 100065; CAS# 524-95-8
Dimethyl Sulfoxide (DMSO)	Fisher Scientific	Cat# BP231-100; CAS# 67-68-5
Experimental models: Organisms/strains		
D. melanogaster: MS1096-GAL4, UAS Dcr2: w[1118] P{w[+mW.hs]=GawB}Bx[MS1096]; P{w[+mC]=UAS-Dcr-2.D}2	Bloomington Drosophila Stock Center (BDSC)	BDSC: 25706 FlyBase: MS1096: FBti0002374, Dcr2: FBti0100275
D. melanogaster: UAS-Dcr2; Engrailed-Gal4; UAS-GFP: P{w[+mC]=UAS-Dcr-2.D}1, w[1118]; P{w[+mW.hs]=en2.4-GAL4}e16E, P{w[+mC]=UAS-2xEGFP}AH2	Bloomington Drosophila Stock Center (BDSC)	BDSC: 25752 FlyBase: Dcr2: FBti0101430, en-Gal4: FBti0003572, GFP: FBti0026662
D. melanogaster: UAS-RyR^{RNAi}: y[1] v[1]; P{y[+t7.7] v[+t1.8]=TRiP.JF03381}attP2	Bloomington Drosophila Stock Center (BDSC)	BDSC: 29445 FlyBase: FBti0129073
D. melanogaster: UAS-Piezo::GFP: w[*]; P{w[+mC]=UAS-Piezo.GFP}IIA-2/CyO; MKRS/TM6B, Tb[1]	Bloomington Drosophila Stock Center (BDSC)	BDSC: 58772 FlyBase: FBti0164866
D. melanogaster: UAS-Piezo::GFP: w[*]; sna[Sco]/CyO; P{w[+mC]=UAS-Piezo.GFP}IIIA/TM6B, Tb[1]	Bloomington Drosophila Stock Center (BDSC)	VDRC: 58773 FlyBase: FBti0164869
D. melanogaster: Pbac Piezo: w[*]; PBac{w[+mC]=RB5.WH5}Piezo[KO]	Bloomington Drosophila Stock Center (BDSC)	VDRC: 58770 FlyBase: FBti0147345
D. melanogaster: UAS-Piezo.FLAG: w[*]; wg[Sp-1]/CyO; M{RFP [3xP3.PB] w[+mC]=UAS-Piezo.FLAG}ZH-86Fb/TM6B, Tb[1]	Bloomington Drosophila Stock Center (BDSC)	BDSC: 95296 FlyBase: FBti0227228
D. melanogaster: Piezo-EGFP tagged: y[1] w[67c23]; Mi{PT-GFSTF.0}Piezo[MI04189-GFSTF.0]	Bloomington Drosophila Stock Center (BDSC)	BDSC: 60209; FlyBase: FBti0178581
D. melanogaster: UAS-Piezo^{RNAi}: P{KK101815}	Vienna Drosophila Resource Center (VDRC)	VDRC: 105132 FlyBase: FBgn0025998
D. melanogaster: UAS-Piezo^{RNAi}: P{GD993}	Vienna Drosophila Resource Center (VDRC)	VDRC: 2796 FlyBase: FBgn0025998
D. melanogaster: Nub-GAL4, UAS-GCaMP6f: nub-GAL4,UAS-GCaMP6f/CyO	Brodskiy et al. 2019 https://doi.org/10.1016/j.bpj.2019.01.007	N/A

(*Continued on next page*)

Continued

REAGENT or RESOURCE	SOURCE	IDENTIFIER
D. melanogaster: Apterous-Gal4; UAS-GFP: y w hsflp; apG4/CyO; UAS-GFP	Gift from Conrad Basler	N/A
D. melanogaster: PBac{RB}Piezo^{e00109}	Harvard	N/A
D. melanogaster: PBac{WH}Piezo^{f02291}	Harvard	N/A
Software and algorithms		
Fiji	Schindelin et al.[93]	https://fiji.sc
Matlab 2021b	Mathworks	https://www.mathworks.com/products/matlab.html

RESOURCE AVAILABILITY

Lead contact

Further information and requests for resources and reagents should be directed to and will be fulfilled by the lead contact, Jeremiah Zartman (jzartman@nd.edu).

Materials availability

This study did not generate new unique reagents.

Data and code availability

An open-source implementation of the computational model and all source codes related to the figures are available on GitHub (https://github.com/MulticellularSystemsLab/Piezo-manuscript-resouces). Data reported in this paper will be shared by the lead contact upon request.

EXPERIMENTAL MODEL AND SUBJECT DETAILS

Fly stocks and culture

Drosophila melanogaster were grown and maintained in a 25°C incubator with a twelve-hour light cycle. Virgins were collected twice a day from the bottles used as farms from Gal4 driver lines. Virgins were crossed with males that carry the indicated UAS-transgene constructs with the gene of interest in a ratio of female to male of 15:5. The crosses were staged for 8 hours to ensure the collection of physiologically correct aged 3rd instar larvae. Wandering 3rd instar larvae, regardless of sex, were dissected to harvest the wing imaginal discs. Adult flies were collected upon eclosion for wing analysis. Both male and female F1 larvae and pupae were sorted based on genetic crossing schemes to ensure correct genotypic expression. Adult progenies were collected 24 hours after eclosion and separated by sex to quantify the wings.

METHOD DETAILS

Live imaging to study cell division

Wing imaginal discs dissected out of third instar crawling larvae on day 6 after egg laying (AEL). The tissues were immediately mounted into polyethylene terephthalate laminate (PETL) microfluidic devices for imaging with the constant flow of media[94]. The devices were then loaded onto the microscope and culture media was introduced via microfluidic flow from syringes and a syringe pump (Harvard Apparatus). Several media were used including various concentrations of Yoda1 that were added to a supplemented Grace's cocktail medium[95] containing Grace's insect medium, Bis Tris, fetal bovine serum (FBS), penicillin and streptomycin, and 20-Hydroxyecdysone was introduced via microfluidic flow after the initial imaging time point. The initial few time points allowed for control within the disc and between discs pre-treatments. Images were acquired with a Spinning Disc Confocal Microscope (Nikon/Andor, custom). Full z-stack (~120 images) was taken every 6 minutes for 4-6 h (Videos S7 and S8), and a 40x magnification was used. Once collected, images then were opened in Fiji[93], and brightness contrast was enhanced for image preparation. Dividing cells (rounded) were counted manually, using previous/following timestamps to confirm mitotic status.

Wing disc immunohistochemistry and mounting

Wing imaginal discs were dissected from 3rd instar *Drosophila* larvae in intervals of 20 min. Fixation was performed on dissected wing discs in ice cold 10% neutral-buffered formalin (NBF) for 30 min in PCR tubes. Fresh PBT (PBS with 0.03% v/v Triton X-100) was used to rinse the wing discs thrice immediately following fixation. Tubes containing wing discs were then placed on a nutator for 10 minutes at room temperature and then rinsed again with PBT; this step was repeated for a total of three nutation/rinsing intervals. PBT from the final rinse was removed and 250 μL of 5% normal goat serum (NGS) in PBS was added to each PCR tube. Tubes were then placed

on a nutator for 30 minutes at room temperature. NGS was replaced with 250 μL of a primary antibody mixture prepared in 5% NGS solution. Next, tubes were placed on a nutator at 4 °C overnight. Three quick rinses were then performed as was done after fixation. Tubes were placed on a nutator for 20 minutes followed by PBT rinsing; repeated for a total of three nutation/rinsing intervals. After removing the PBT from the final rinse, 250 μL of a secondary antibody mixture, prepared in 5% NGS solution, was added. Tubes were then placed on a nutator for 2 hours at room temperature. Three subsequent quick rinses were performed as before. Tubes were then placed on a nutator for 20 minutes at room temperature and then rinsed with PBT for a total of three intervals. Wing discs were incubated at 4°C for an overnight wash and finally mounted on slides using Vectashield mounting medium.

Confocal microscopy

Wing imaginal discs were imaged using a Nikon Eclipse Ti confocal microscope with a Yokogawa spinning disc, and a Nikon A1R-MP laser scanning confocal microscope. For the two confocal microscopes, image data were collected on an IXonEM+colled CCD camera (Andor Technology, South Windsor, CT) using MetaMorph v7.7.9 software (Molecular Devices, Sunnyvale, CA) and NIS-Elements software, respectively. Discs were imaged throughout the entire depth of z-planes with a step size of 0.8-1 μm, depending on sample thickness, with a 40x and 60x oil objective with 200 ms exposure time, and 50 nW, 405 nm, 488 nm, 561 nm, and 640 nm laser exposure at 44% laser intensity. The imaging was performed from apical to basal surface so that peripodial cells were imaged first followed by the columnar cells of the wing disc. Optical slices were taken at distances equaling half the compartment length.

Confocal imaging data were processed and analyzed in Fiji according to previously established methodology[96], e.g., for the E-Cadherin antibody staining data, a rolling ball background subtraction with a ball radius of 50 pixels was first used to subtract the background from the images. Non-specific low-intensity signals were eliminated through intensity thresholding. A cross-sectioning line was drawn along the apical surface of the pouch region in the center of the wing disc, and the "Plot Profile" tool was employed to extract intensity values at multiple points. We next averaged the intensities along the pouch AP axis over ten equally spaced regions. Subsequently, the intensities extracted at all points were normalized based on the maximum integrated fluorescence within a subregion. Finally, these normalized intensity values were averaged across multiple independent samples to determine the mean and standard deviation, as depicted in Figure 3C. Similar analysis was performed for pMyoII. However, for pMyoII, the cross-sectioning line was drawn along the anterior or posterior compartment, slightly away from the center of the wing disc (Figure S4C).

In Figure 4, we manually assessed the ratio of antibody-stained cells to nuclei (DAPI) co-stained to quantify apoptotic and mitotic cells labeled with *Drosophila* caspase-1 (DCP-1) and Phospho-Histone H3 (PH3) antibodies in Figure 4, respectively. By comparing these counts, we derived the apoptotic and mitotic index by dividing the total number of dying or proliferating cells in the pouch region by the pouch area, which provided a robust measure of cell death or proliferation activity within the wing disc pouch.

Laser ablation and semi-automated recoil analysis

For the laser ablation experiments, *Drosophila* wing discs were cultured in Supplemented Grace's Medium supplemented with Bis-Tris, Penn-Strep, and FBS, low 20-hydroxyecdysone[95]. To achieve a final concentration of 0.1 mM Yoda1, 5 μM GsMTx4, or corresponding vehicle control (DMSO for Yoda1, water for GsMTx4), drug/control was added, and discs were pretreated for 90 minutes before loading into a PETL microfluidic device for ablation and imaging[94]. A dye cell laser (MicroPoint, Andor) was tuned to create a ~1 μm diameter ablation along the edge of a cell. The laser intensity was calibrated at the beginning of each day to only ablate the selected area (30-70% power). Imaging was automated such that 100x images were taken every 500 ms for 15-30 seconds, with the ablation occurring at the third time point[97]. The images were then imported to Fiji (NIH, ImageJ) Software and contrast and brightness were increased to decrease background noise and make cell bonds clear. A line was then drawn parallel to the ablated bond to take a kymograph representation of the moving neighboring tricellular junctions. Kymographs were fed into a custom MATLAB script that measured the distances between local maxima of image intensity, averaging across 5 neighboring pixels to smooth the curves, reducing noise. The resultant maxima distances were then normalized to their initial length in pixels and the fraction increase from the initial length was recorded. Averages were taken across the samples to create Figure S5 and Videos S9–S11.

We also pursued a secondary confirmation that mechanosensitive channels like Piezo, impact tension levels in the wing disc. We performed laser ablation experiments after treating the wing discs with the pharmacological inhibitor of Piezo, GsMTx4, or activator, Yoda1. Here, we have specified the recoil velocity in terms of change in length over time, instead of direct force calculation in terms of mechanical properties. We normalized the lengths using pixels as units and reported the length changes in terms of fraction initial length to normalize different lengths of cell edges. The fraction changes in length are proportional to F_0/u, where F_0 is the tensile force present at the junction before ablation, and μ is the viscosity coefficient related to the viscous drag of the cell cytoplasm[97]. In this secondary laser ablation experiment, we assume that any viscosity changes do not impact the overall changes on forces in the tissue. Additional experimentation and simulations will be required to decouple the effects of changes in length to cytoskeletal properties including viscosity.

Quantification of Ca^{2+} spikes

Quantification of the live imaging data was performed using a software, CaImAn[98] which performs both motion correction and source extraction of the calcium signals. This follows the typical workflow of calcium image analysis[99]. The source extraction was optimized by changing the parameters of the software to ensure an efficient and close to reality extraction of the fluorescent profile. After source

extraction, the fluorescence profile was extracted and post calculations of the parameters that describe the system were developed using the mathematical Python package, SciPy[100]. The features that were extracted from the signaling profile are: (1) number of peaks, (2) frequency of the peaks, (3) width of half maximum of the peaks and (4) average height of the peak. Afterward, plotting and statistical analysis of the extracted data were performed using python packages Matplotlib, for the plotting, and statsmodels and scikit-learn, for the statistical analysis[101–103].

As per the two-pool model[62], the binding of an IP_3 molecule on an IP_3 receptor (IP_3R) located on the endoplasmic reticulum (ER) provokes the liberation of Ca^{2+} into the cytosol. This increase in Ca^{2+} triggers the release of Ca^{2+} from another Ca^{2+}-sensitive source. Cytosolic Ca^{2+} decreases due to pumping into the Ca^{2+}-sensitive store and extrusion from the cell. The IP_3 is assumed to be a constant in the model. The model can be represented by the following equations:

$$\frac{dZ}{dt} = V_{in} - V_2 + V_3 + k_f Y - kZ$$

$$\frac{dY}{dt} = V_2 - V_3 - k_f Y$$

with,

$$V_{in} = \nu_0 + \nu_1 \beta$$

$$V_2 = V_{M2}\frac{Z^n}{Z^n + K_2^n}$$

$$V_3 = V_{M3}\frac{Z^p}{Z^p + K_A^p}\frac{Y^m}{Y^m + K_R^m}$$

In these equations, Z represents the cytosolic Ca^{2+} while Y is the concentration of Ca^{2+} in an IP_3 insensitive store. V_{in} represents the total constant entry of Ca^{2+} in the cytosol; it includes the influx ν_0 from the extracellular medium and the IP_3-stimulated Ca^{2+} release $\nu_1\ \beta$. Whereas V_2 and V_3 are, respectively, the rates of pumping into and release from the Ca^{2+}-sensitive zone, with V_{M2} and V_{M3} determining the maximum rates of these processes. K_2, k_f and K_A are the threshold constants of pumping, release, and activation, while n, m and p are the Hill coefficients. $k_f Y$ and kZ refer to the passive efflux from Ca^{2+}-sensitive store and cytosol.

Quantification of epithelial packing

Volumetric images were first corrected manually to remove peripodial cell boundaries from each z-slice. Slices were chosen to contain only the cells located at the apical surface. Antibody staining against *Drosophila* E-Cadherin (DCAD2) was carried out to mark the cell boundaries at the apical surface. Background noise was then subtracted from these images using the CSBDeep plugin[104] in FIJI. A maximum intensity z projection was taken next to get an approximation of cell boundaries in the apical surface. We next used EPySeg[105] to segment out the cell boundaries. The segmentation masks were next imported to MATLAB for further quantification. We first used the regionprops function in MATLAB to quantify cell areas and centroids of each cell. Anisotropy was estimated through the calculation of texture tensor as described in LeGoff et. al[106]. For estimating the polygon nature/number of neighbors for each cell in the epithelia the following methodology was used. To check if two cells are neighbors of one another, we used a dilation filter on both cells. The dilation was carried out using a circular element with a radius equaling the width of the cell boundaries measured manually in FIJI. If the dilation operation resulted in a single object post application of the filter, it implies that the two objects are neighbors of each other. For each cell, the operation was carried out on all possible cell pairs to estimate the total number of neighbors. We then used the number of neighbors to define the cell's polygon class.

Vertex model of epithelial growth

The total energy of the epithelia is modeled as described in Farhadifar et. al[79]. where surface tension area elasticity and perimeter-based contractility functions are defined.

$$E_{total} = \sum_{ij} \lambda_{ij} l_{ij} + \frac{1}{2}\sum_i K_i (A_i - A_0)^2 + \frac{1}{2}\sum_i \Gamma_i (P_i)^2$$

where λ (= 0.1) and ℓ (= 1) denotes the desired cell edge tension and length of the cell, respectively. Parameter λ can be reduced biologically by increasing the cell-cell adhesion. Another way of reducing this parameter is through a reduction in actomyosin contractility. Cells are also considered to be elastic, and their energy is calculated through an approximation of elastic energy. K_i (= 1) denotes the face elasticity and is multiplied by the square of difference between current (A_i) and preferred apical area (A_o = 1) of the cell. Lastly, we define the contractility of cell perimeter (Γ = 0.04) to model actomyosin-mediated contractility.

All the energy functions are implanted using an open-source Python package Tyssue[107]. Growth within the tissue has been modeled following Farhadifar et al.[79]. The cells within the tissue are assigned a growth rate with added noise. The growth is further

patterned and is higher at the center (= 0.04) and lower at the boundaries (= 0.01). Minimum and maximum growth rates are defined and the growth rate of a cell within the pouch is computed based on linear regression. The assumption of patterned growth is based on the work done by Mao et al. where they have shown that growth is patterned in the *Drosophila* wing imaginal disc and decreases as one moves away from the center of the pouch[108]. When cells reach a critical volume ($V_{cutoff,division}$), they split using Tyssue's inbuilt cell division module. Apoptosis within the epithelia has been modified to add to the effect of contraction on neighboring cells. This is achieved through a two-step approach of modeling apoptosis[109]. In the first step, cells with area less than a defined area ($V_{cutoff,apoptosis}$) are reduced in volume with a fixed rate (= A_i/1.2), until the cell's apical area reaches a critical value ($V_{cutoff,elimination}$). During this shrinking process the neighboring cells are also pulled and contracted with a defined radial tension (= 0.02) using Tyssue's inbuilt module. In the second step of process, cells are eliminated based on the number of neighbors. If the number of neighbors is less than or equal to three, they are removed from the epithelia. If the number of neighbors is greater than three, a rearrangement occurs along the shortest side. Rearrangements occur based on edge lengths. If the length of a particular edge of a cell is less than a particular threshold value (= 0.005) rearrangement happens along the shortest side.

Statistical tests

A t-test[110] (t-stat, p-val) was used to compare population means while Bartlett's test[111] (F-stat, F-test, p val) was utilized to assess if the variances of the groups compared are statistically significant. Finally, we also report Cohen's d[112] to measure the effect of sample size on t-test statistics. We adjusted the alpha values calculated using the Bonferroni correction method. We report all statistical tests in Tables S2–S7.